$G_0\Delta W$ theory: Quasiparticle properties of two-dimensional semiconductors physisorbed on graphene

Lovro Anto Barišić[1] and Vito Despoja[2,3,*]

[1]*Laboratoire de Physique de l' École normale supérieure, ENS, Université PSL, CNRS, Sorbonne Université, Université Paris Cité, F-75005 Paris, France*

[2]*Centre for Advanced Laser Techniques, Institute of Physics, Bijenička 46, 10000 Zagreb, Croatia*

[3]*Donostia International Physics Center (DIPC), P. Manuel de Lardizabal, 4, 20018 San Sebastián, Spain*

(Received 26 September 2023; revised 1 December 2023; accepted 11 December 2023; published 2 January 2024)

The theoretical formulation that enables calculation of quasiparticle properties of two-dimensional (2D) semiconductors physisorbed at another 2D crystal is presented. The formulation is applied to calculate the induced correlation self-energy $\Delta\Sigma^{C,S}(\omega)$ and spectral line shapes of the valence and conduction bands in MoS_2, WS_2, and hBN caused by nearby pristine or doped graphenes. It is shown that graphene negligibly shifts the valence and conduction bands in MoS_2 and WS_2 causing the maximum band gap reduction of $-\Delta E_g \sim 150$ meV. The influence of graphene on hBN band structure is stronger, causing the band gap reduction of $-\Delta E_g \sim 700$ meV. The larger number of graphene layers or doped graphene negligibly affect the valence and conduction bands shifts, which are also approximately rigidly shifted along the entire Brillouin zone. The spatially dependent induced self-energy of point charge $\Delta\Sigma^{S@2D}(z_0)$ (image potential) is much weaker in MoS_2 or WS_2 than in hBN indicating that transition-metal dichalcogenides electronic screening efficiently cancel substrate polarization effects and thus protect the band structure from substrate influences. When graphene is brought next to the hBN it induces satellites in the hBN conduction and valence bands. Graphene's interband $\pi \rightarrow \pi^*$ transitions induce weak π satellites, while Dirac plasmon, present in the doped graphene, induces more intensive D plasmaron, which might be observed in photoemission measurements.

DOI: 10.1103/PhysRevB.109.035301

I. INTRODUCTION

The relatively simple manipulation of the electronic and optical properties of the semiconducting two-dimensional (2D) crystals made them very attractive for applications in microelectronics [1–4], optoelectronics, photonics [5–7], as photodetectors, sensors, and in telecommunications [7–9]. Even since 2011, the 2D materials are being tested as transistors, light-emitting diodes (LEDs), solar cells, photodetectors, or quantum emitters [10].

The 2D crystals band gap and consequently the optical gap can be modified quite effectively in many different ways. For example, by stacking the different or the same types of 2D materials in van der Waals (vdW) heterostructures [11–15], by applying uniaxial strain [16], by intercalation of multilayered 2D crystals by organic molecules [17], or simply by placing the 2D crystals in different dielectric environments [2,15,18–24].

The possibility of manipulation of the quasiparticle band gap and exciton binding energy in 2D materials using different dielectric substrates is intensively explored in the last ten years. Many different groups were engaged to study the influence of various substrates such as graphene (Gr), graphene bilayers (Gr-BL), graphene trilayers (Gr-TL), graphite, hBN, SiO_2, Au(111), and many others on the band gaps and exciton binding energies in various TMD single layers (SLs), and these were mostly MoS_2 or WS_2 [2,18,22,24–29]. Considering that the absolute band gap in freestanding 2D crystal (vacuum band gap) is difficult to determine experimentally, mainly the change in the gap is measured, relative to some reference value, which is the gap at weakly polarizable substrate, such as SiO_2 or hBN. For example, the angle-resolved photoemission-spectroscopy (ARPES) measurements show that WS_2 band gap decreases about 140 meV on a graphite substrate as compared to a hexagonal boron nitride substrate, and that WS_2 conduction and valence bands are mostly rigidly shifted along the Brillouin zone [24]. Interestingly, optical measurements on the Gr/hBN/WS_2 composite show that graphene reduces the WS_2 band gap (relative to the band gap at hBN) by only 60 meV [23]. Electric transport measurements show that the band gap of MoS_2 on a fluoropolymer substrate is about 180 meV larger than the band gap in MoS_2 on hBN substrate [2]. However, the absolute band gap change (induced by a substrate) could in principle be determined by taking the results of the *GW* calculations as a reference, even though these results are not always consistent.

For example, the reported G_0W_0 band gaps in MoS_2 vary from 2.5 eV [2], 2.6 eV [30,31], 2.7 eV [27], up to more than 2.8 eV [29,32]. Taking into account that the band gap of MoS_2 on graphite [measured by scanning tunneling spectroscopy (STS)] is $E_g \sim 2.15$ eV [25], and above G_0W_0 estimations, the MoS_2 band gap reduction caused by graphite can vary from 350 meV−650 meV. Some very recent systematic research says that the G_0W_0 fundamental gap in MoS_2 is sensitive on a multitude of parameters, such as the geometrical parameters

*vdespoja@ifs.hr

(cell parameters and atomic coordinates), the choice of the initial XC functional, the choice of truncated potential, the inclusion of spin-orbit coupling, and maybe the most important, the treatment of the $\mathbf{q} = 0$ singularity in $\mathbf{q}$ integration. Depending on the choice of these parameters the fundamental band gap can vary even between 2.31 and 2.97 eV [33].

The G_0W_0 band gap in self-standing WS_2 vary from 2.43 eV [34] to 2.73 eV [35], while some estimations based on optical measurement and exciton-binding energy shows that WS_2 band gap at SiO_2 surface is 2.4 eV [18]. In the same paper it is shown that coverage by Gr-SL, Gr-BL, or Gr-TL causes an additional band gap reduction of about 140 meV, while if WS_2 is encapsulated by two graphenes gap reduction increases to 300 meV. From this it can also be concluded that SiO_2 negligibly reduces the gap and that graphene sandwich reduces the gap approximately twice. This is consistent with another joint theoretical/experimental findings showing that MoS_2 band gap, regardless of whether it is physisorbed on Gr-SL, -BL, or -TL, changes about 300 meV, and at graphite substrate about 500 meV, while at hBN and SiO_2 substrates the gap changes are negligible [28]. Another investigation shows that hBN surface reduces the MoS_2 band gap (relative to gap in vacuum) by about 140 meV [2] or 160 meV [29], while SiO_2 and Au(111) surfaces by 140 meV and 640 meV [22,29], respectively. The band structure modifications including appearance of polaron satellites in various hBN/graphene heterostructures using angle-resolved photoemission spectroscopy are recently researched in detail [36–39]. We will do the same here, but we will concentrate on the appearance of plasmonic satellites in the hBN band structure.

The theoretical calculations of WS_2 or MoS_2 band gaps on different substrates, using different $G_0\Delta W$ methods support the above experimental results very well [2,22,24,27–29]. The supercell $G_0\Delta W$ methods, in which the 2D crystal and the substrate (e.g., another 2D crystal) forms the single crystal [2,28,29] shows excellent agreement with experiments. Moreover, these results are very useful for benchmarking the other methods in which the 2D crystal/substrate orbital hybridization is neglected [18,40]. The problem of supercell method is that it can be, due to the large unit cells, computationally very demanding reducing the accuracy of the results. It seems that the supercell method overestimates the experimental result, which is best seen on the example of MoS_2 [28] where the calculated band gap reduction caused by graphene multilayers is about 400 meV, which is about three times larger than band gap reduction measured at the same conditions in WS_2 [18] or five times larger than the gap change measured in $MoSe_2$/Gr-BL composite [26]. The band gap renormalizations are also simulated using $G_\Delta W$ method where the orbitally decoupled substrate is described by induced Coulomb interaction $\Delta W = W(\epsilon_{\text{eff}}) - W(\epsilon_{\text{eff}} = 1)$, where the effective background dielectric constant is $\epsilon_{\text{eff}} = (1 + \epsilon_S)/2$ and where ϵ_S is substrated dielectric constant [22,24,27,41]. The disadvantage of this method is that it also overestimates the band gap reduction caused by the substrate. The reasons for that is that the ϵ_{eff} is constant, i.e., frequency, momentum, and spatially independent. On the other hand, inclusion of the lateral nonlocality, i.e., momentum ($\mathbf{Q}$) dependence, and perpendicular spatial dependence, through the exponential factor $e^{-|\mathbf{Q}|(z+z')}$, reduce the substrate-induced Coulomb interaction and thus band gap reduction. For example, in Ref. [27] the MoS_2/hBN gap reduction is 180 meV, which overestimate results 30–160 meV presented in Refs. [2,28,29]. Also, in this method ϵ_S is usually treated as a free parameter tuned to satisfy the experimental band gap [22,24]. Finally, the *GdW* method [42] (the modified G_0W_0 method applied to bulk crystals, where instead of subtracting the local V_{XC} operator from G_0W_0 self-energy, it is shown to be much more efficient to subtract the metallic component of self-energy iG_0W_{metal}) is also applied to study influence of different substrates on the quasiparticle properties in MoS_2 [29].

Here we formulate the correlation self-energy induced by the proximity of another 2D crystal or a composite of 2D crystals $\Delta\Sigma_{C,S} = iG_0\Delta W$. The induced Coulomb interaction in 2D crystal/substrate composite is $\Delta W = W[V + \Delta V] - W[V]$, where V and $V + \Delta V$ are bare and substrate screened Coulomb propagators, respectively. The momentum, frequency, and spatially dependent induced propagator ΔV is expressed in terms of 2D dielectric functions $\epsilon_{2D}(\mathbf{Q}, \omega)$ of the 2D crystals that build the substrate [40]. This theory is applied to study the quasiparticle properties, such as shifts and spectral line shapes, of the valence and conduction bands in WS_2, MoS_2, and hBN SLs, induced by various substrates, such as pristine and doped graphenes, graphene multilayers, and hBN. It should be noted here that the quasiparticle properties of various TMDs at multilayered hBN substrates are recently studied using dielectric embedding *GW* approach [43]. This method also neglects the orbital overlap, however, it is more sophisticated because it includes the crystal local field effect in the substrate response. Very similar to the $G\Delta W$ method, where the change in the screened Coulomb interaction ΔW is derived using the quantum-electrostatic heterostructure (QEH) model [40], is used to calculate the gap change in many multilayered vdW 2D crystals [44]. Our obtained results are compared with many of those recent experimental and theoretical results.

The rest of the paper is organized as follows. In Sec. II we present the geometry of the system and derivation of substrate-induced correlation self-energy $\Delta\Sigma^{C,S}$, in Sec. III we present the computational details. In Sec. IV we present the results, and the conclusions are presented in Sec. V.

II. THEORETICAL FORMULATION

In the next three theoretical sections, we start with the standard formulas within G_0W_0 approach for the exchange-correlation self-energy Σ_{XC} in 2D crystals (using the truncated Coulomb intercation proposed in Ref. [45]). Finally we formulate the induced correlation self-energy $\Delta\Sigma_{C,S}$ caused by interaction of 2D crystals with the adjacent substrate. All theoretical derivations were made using the zero temperature ($T = 0$) formalism and atomic units are used $\hbar = 1$, $e = 1$, and $m = 1$.

A. Standard G_0W_0 approximation applied to calculate the Green's function of arbitrary quantum state $|n\rangle$

Here we will first introduce some standard terms so that later the theory can be more easily applied to 2D crystals.

The Hamiltonian describing N electrons moving in some local potential $v(\mathbf{r})$ is

$$H_0 = \sum_{i=1}^{N} H_0(\mathbf{r}_i), \tag{1}$$

where

$$H_0(\mathbf{r}_i) = -\tfrac{1}{2}\nabla_i^2 + v(\mathbf{r}_i). \tag{2}$$

Since the Hamiltonian H_0 is separable, the problem can be reduced to problem of one electron moving in the local potential $v(\mathbf{r})$. Therefore, we suppose that the electrons fill the one-particle states $\{\phi_n(\mathbf{r}), E_n\}$ that satisfy Schrödinger equation:

$$H_0\phi_n(\mathbf{r}) = E_n\phi_n(\mathbf{r}). \tag{3}$$

The propagation (or Green's function) of an electron or hole of energy ω from point $\mathbf{r}'$ to point $\mathbf{r}$ is then

$$G_0(\mathbf{r}, \mathbf{r}', \omega) = \sum_n \phi_n(\mathbf{r})\phi_n^*(\mathbf{r}')G_n(\omega), \tag{4}$$

where the propagator of an electron or hole of energy ω in quantum state $|n\rangle$ is

$$G_n(\omega) = \frac{1 - f_n}{\omega - E_n + i\delta} + \frac{f_n}{\omega - E_n - i\delta}. \tag{5}$$

Here $f_n = \theta(E_F - E_n)$ represents the Fermi-Dirac distribution at $T = 0$ and $\delta = 0^+$. If the Coulomb interaction between electrons is switched on, the Hamiltonian of the system becomes

$$H = H_0 + \frac{1}{2}\sum_{i\neq j}^{N} V(\mathbf{r}_i, \mathbf{r}_j), \tag{6}$$

where

$$V(\mathbf{r}, \mathbf{r}') = \frac{1}{|\mathbf{r} - \mathbf{r}'|}, \tag{7}$$

represents the propagator of bare Coulomb interaction. If the electron-electron interaction is considered as small perturbation then according to Hedin's scheme [46,47] and standard many-body perturbation theory [48–52] the propagator of an electron or hole in quantum state $|n\rangle$ becomes

$$G_n(\omega) = \frac{1}{\omega - E_n - \Sigma_n(\omega)}, \tag{8}$$

where the self-energy of the quantum state $|n\rangle$ in diagonal approximation is

$$\Sigma_n(\omega) = \Sigma_n^{\mathrm{H}} + \Sigma_n^{\mathrm{XC}}(\omega). \tag{9}$$

Here, the Hartree self-energy is

$$\Sigma_n^{\mathrm{H}} = \sum_m f_m \int d\mathbf{r} \int d\mathbf{r}' \times \phi_n^*(\mathbf{r})\phi_n(\mathbf{r})V(\mathbf{r}, \mathbf{r}')\phi_m^*(\mathbf{r}')\phi_m(\mathbf{r}'), \tag{10}$$

and exchange-correlation self-energy is

$$\Sigma_n^{\mathrm{XC}}(\omega) = \int d\mathbf{r}d\mathbf{r}'\phi_n^*(\mathbf{r})\Sigma_{\mathrm{XC}}(\mathbf{r}, \mathbf{r}', \omega)\phi_n(\mathbf{r}'). \tag{11}$$

The exchange-correlation self-energy operator in G_0W_0 approximation is [46]

$$\Sigma_{\mathrm{XC}}(\mathbf{r}, \mathbf{r}', \omega) \approx \Sigma_{\mathrm{XC}}^0(\mathbf{r}, \mathbf{r}', \omega) = i\int_{-\infty}^{\infty} \frac{d\nu}{2\pi} e^{i\nu\tau} G_0(\mathbf{r}, \mathbf{r}', \omega + \nu)W_0(\mathbf{r}', \mathbf{r}, \nu), \tag{12}$$

where $\tau = 0^+$. In terms of Hilbert-Kramers–Kronig relations the time-ordered screened Coulomb interaction W_0 can be written as [47]

$$W_0(\mathbf{r}, \mathbf{r}', \omega) = V(\mathbf{r}, \mathbf{r}') + \int_0^{\infty} d\omega' \times \left\{ \frac{S_0(\mathbf{r}, \mathbf{r}', \omega')}{\omega - \omega' + i\eta} - \frac{S_0(\mathbf{r}', \mathbf{r}, \omega')}{\omega + \omega' - i\eta} \right\}, \tag{13}$$

where the potential-potential correlation function is

$$S_0(\mathbf{r}, \mathbf{r}', \omega) = \int_{-\infty}^{\infty} dt e^{i\omega t} \langle \Phi(\mathbf{r}, t)\Phi(\mathbf{r}', 0)\rangle.$$

Here the potential operator is defined as

$$\Phi(\mathbf{r}, t) = \int d\mathbf{r}_1 V(\mathbf{r}, \mathbf{r}_1)\rho(\mathbf{r}_1, t),$$

where $\rho = \Psi^*\Psi$ is electron density operators, and the averaging goes over the interacting ground state. If we assume next symmetry $S_0(\mathbf{r}', \mathbf{r}, \omega) = S_0(\mathbf{r}, \mathbf{r}', \omega)$ then the correlation function is real $[S_0(\mathbf{r}, \mathbf{r}', \omega) \in \mathbb{R}]$ and it can be, according to Eq. (13), connected with the imaginary part of the time-ordered screened Coulomb interaction as

$$S_0(\mathbf{r}, \mathbf{r}', \omega) = -\frac{1}{\pi}\mathrm{Im}W_0(\mathbf{r}, \mathbf{r}', \omega)\theta(\omega). \tag{14}$$

Relation (14) is also known as fluctuation-dissipation theorem because it connect the correlations S_0 and energy dissipations -ImW_0 (spectrum of electronic excitations in the studied system). After the spectral representation (13) and free Green's function (4)–(5) are inserted in self-energy (12), integration over ν is performed and then all is inserted in Eq. (11), the exchange-correlation self-energy of the quantum state $|n\rangle$ becomes

$$\Sigma_n^{\mathrm{XC},0}(\omega) = \Sigma_n^{\mathrm{X}} + \Sigma_n^{\mathrm{C},0}(\omega). \tag{15}$$

The bare Coulomb interaction in (13) provides the Fock or exchange self-energy

$$\Sigma_n^{\mathrm{X}} = -\sum_m f_m \int d\mathbf{r} \int d\mathbf{r}' \times \phi_n^*(\mathbf{r})\phi_m(\mathbf{r})V(\mathbf{r}', \mathbf{r})\phi_m^*(\mathbf{r}')\phi_n(\mathbf{r}'), \tag{16}$$

while the induced Coulomb interaction provides the correlation self-energy

$$\Sigma_n^{\mathrm{C},0}(\omega) = \sum_m \int d\mathbf{r} \int d\mathbf{r}'\{(1 - f_m)\,\phi_n^*(\mathbf{r})\phi_m(\mathbf{r}) \times \Gamma_0(\mathbf{r}', \mathbf{r}, \omega - E_m)\phi_m^*(\mathbf{r}')\phi_n(\mathbf{r}') - f_m\,\phi_n^*(\mathbf{r})\phi_m(\mathbf{r}) \times \Gamma_0(\mathbf{r}', \mathbf{r}, E_m - \omega)\phi_m^*(\mathbf{r}')\phi_n(\mathbf{r}')\}, \tag{17}$$

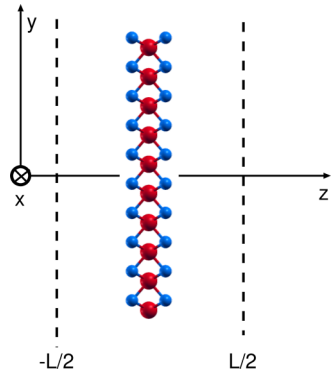

FIG. 1. Geometry of the system. The 2D crystals are periodically repeated so that they form a superlattice of the unit cell L in z direction.

where we introduce so-called correlation propagator

$$\Gamma_0(\mathbf{r},\mathbf{r}',\omega)=\int_0^\infty d\omega' \frac{S_0(\mathbf{r},\mathbf{r}',\omega')}{\omega-\omega'+i\delta}. \tag{18}$$

The main quantity entering the correlation self-energy is time-ordered screened Coulomb interaction satisfying next Dyson's equation

$$W_0(\mathbf{r},\mathbf{r}',\omega) = V(\mathbf{r},\mathbf{r}')+\int d\mathbf{r}_1 d\mathbf{r}_2 V(\mathbf{r},\mathbf{r}_1)\chi_0(\mathbf{r}_1,\mathbf{r}_2,\omega)W_0(\mathbf{r}_2,\mathbf{r}',\omega), \tag{19}$$

where time-ordered random phase approximation (RPA) irreducible polarizability is

$$\chi_0(\mathbf{r},\mathbf{r}',\omega)=\sum_{nm}\phi_n^*(\mathbf{r})\phi_m(\mathbf{r})\phi_m^*(\mathbf{r}')\phi_n(\mathbf{r}') \times\frac{f_n-f_m}{\omega+E_n-E_m+i\delta sgn(E_m-E_n)}. \tag{20}$$

B. G_0W_0 approximation applied to calculate the Green's function of quantum state $|n,\mathbf{K}\rangle$ in self-standing 2D crystal

Suppose that the 2D crystal occupies the x-y plane and is periodically repeating in the z direction as illustrated in Fig. 1. In such 2D crystal the noninteracting electrons fill the Bloch states, so that the generic base set $\{\phi_n(\mathbf{r}), E_n\}$ should be replaced with Bloch states

$$\begin{aligned}\phi_n(\mathbf{r}) &\rightarrow \phi_{n\mathbf{K}}(\boldsymbol{\rho},z)=\frac{1}{\sqrt{\Omega}}e^{i\mathbf{K}\boldsymbol{\rho}}\,u_{n\mathbf{K}}(\boldsymbol{\rho},z),\\ E_n &\rightarrow E_{n\mathbf{K}};\quad \mathbf{K}\in \mathrm{SBZ},\end{aligned} \tag{21}$$

where Ω is the normalization volume, SBZ denotes surface Brillouin zone, $\mathbf{K}=(K_y,K_y)$ is 2D wave vector, $u_{n\mathbf{K}}(\boldsymbol{\rho}+\mathbf{R},z+L)=u_{n\mathbf{K}}(\boldsymbol{\rho},z)$ is the periodic part of Bloch wave function, $\boldsymbol{\rho}=(x,y)$ is 2D position vector, and $\mathbf{R}=(R_x,R_y)$ is 2D primitive translation vector. Here L is the unit cell in the z direction, as shown in Fig. 1. In Sec. II A index n represented general quantum number but in Bloch states it denotes band index. The Bloch wave functions also satisfy the periodicity in momentum space $\phi_{n\mathbf{K}+\mathbf{G}_\parallel}(\boldsymbol{\rho},z)=\phi_{n\mathbf{K}}(\boldsymbol{\rho},z)$, where $\mathbf{G}=(\mathbf{G}_\parallel,G_z)$ and $\mathbf{G}_\parallel=(G_x,G_y)$ are reciprocal wave vectors. If the Bloch states (21) are self-consistent solution the Kohn-Sham (KS) equation then the electron-electron interaction is already (depending on the choice of the exchange-correlation functional) included in that states. What is certain is that the energies $E_{n\mathbf{K}}$ already contain the exact Hartree energy $\Sigma^{\mathrm{H}}_{n\mathbf{K}}$, so that here we will exclude it from consideration and focus on exchange and correlation contributions $\Sigma^{\mathrm{X}}_{n\mathbf{K}}$ and $\Sigma^{\mathrm{C},0}_{n\mathbf{K}}(\omega)$, respectively. Moreover, the energies $E_{n\mathbf{K}}$ also contain density-functional theory (DFT) exchange-correlation contribution $E^{\mathrm{XC}}_{n\mathbf{K}}$, which needs to be extracted at some point. Here we will first briefly explain how to solve the Dyson equation for propagator W_0, which excludes spurious interaction between the neighboring unit cells within the supercell approach, and then how to use it to determine exchange-correlation self-energy $\Sigma^{\mathrm{XC},0}_{n\mathbf{K}}$. After the Bloch wave functions and energies (21) are inserted in Eq. (20) the irreducible polarizability can be expressed in the form of next Fourier expansion

$$\chi_0(\mathbf{r},\mathbf{r}',\omega) = \frac{1}{L}\sum_{\mathbf{G}}\sum_{\mathbf{G}'}\int_{\mathrm{SBZ}}\frac{d\mathbf{Q}}{(2\pi)^2}e^{i(\mathbf{Q}+\mathbf{G})\mathbf{r}}e^{-i(\mathbf{Q}+\mathbf{G}')\mathbf{r}'}\chi^0_{\mathbf{G}\mathbf{G}'}(\mathbf{Q},\omega), \tag{22}$$

where the matrix of irreducible polarizability is

$$\chi^0_{\mathbf{G}\mathbf{G}'}(\mathbf{Q},\omega)=\frac{2}{\Omega}\sum_{nm}\sum_{\mathbf{K}\in \mathrm{S.B.Z}}(f_{n\mathbf{K}}-f_{m\mathbf{K}+\mathbf{Q}}) \times\frac{\rho_{n\mathbf{K},m\mathbf{K}+\mathbf{Q}}(\mathbf{G})\,\rho^*_{n\mathbf{K},m\mathbf{K}+\mathbf{Q}}(\mathbf{G}')}{\omega+E_{n\mathbf{K}}-E_{m\mathbf{K}+\mathbf{Q}}+i\delta\ \mathrm{sgn}(E_{m\mathbf{K}+\mathbf{Q}}-E_{n\mathbf{K}})}, \tag{23}$$

and where the charge vertices are defined as

$$\rho_{n\mathbf{K},m\mathbf{K}+\mathbf{Q}}(\mathbf{G})=\int_\Omega d\mathbf{r}\ \phi^*_{n\mathbf{K}}(\mathbf{r})e^{-i(\mathbf{Q}+\mathbf{G})\mathbf{r}}\phi_{m\mathbf{K}+\mathbf{Q}}(\mathbf{r}). \tag{24}$$

To avoid spurious interaction with 2D crystal replicas the bare Coulomb potential should be constrained to propagate the interactions only within the one unit of the supercell $z,z'\in[-L/2,L/2]$, i.e., $V\rightarrow V^{\mathrm{C}}$ where

$$V^{\mathrm{C}}(\mathbf{r},\mathbf{r}')=\begin{cases}V(\mathbf{r},\mathbf{r}'); & z \text{ and } z'\in[-L/2,L/2]\\ 0; & z \text{ and/or } z'\notin[-L/2,L/2]\end{cases}. \tag{25}$$

The potential (25) satisfies the following Fourier expansion:

$$V^{\mathrm{C}}(\mathbf{r},\mathbf{r}') = \frac{1}{L}\sum_{G_zG_z'}\int\frac{d\mathbf{Q}}{(2\pi)^2}e^{i\mathbf{Q}(\boldsymbol{\rho}-\boldsymbol{\rho}')}e^{iG_zz-iG_z'z'}V^{\mathrm{C}}_{G_zG_z'}(\mathbf{Q}), \tag{26}$$

where

$$V^{\mathrm{C}}_{G_zG_z'}(\mathbf{Q})=\frac{1}{L}\int_{-L/2}^{L/2}dzdz'e^{-iG_zz}V(\mathbf{Q},z,z')e^{iG_z'z'}, \tag{27}$$

and

$$V(\mathbf{Q},z,z')=v_Qe^{-|\mathbf{Q}||z-z'|},$$

where $v_Q = \frac{2\pi}{|\mathbf{Q}|}$. The Eq. (26) rearranged to be compatible with the expansion of the irreducible polarizability (22) is

$$V^{\mathrm{C}}(\mathbf{r},\mathbf{r}') = \frac{1}{L}\sum_{\mathbf{G}\mathbf{G}'}\int_{\mathrm{SBZ}}\frac{d\mathbf{Q}}{(2\pi)^2}e^{i(\mathbf{Q}+\mathbf{G})\mathbf{r}}e^{-i(\mathbf{Q}+\mathbf{G}')\mathbf{r}'}V^{\mathrm{C}}_{\mathbf{G}\mathbf{G}'}(\mathbf{Q}), \quad (28)$$

where the matrix of bare truncated Coulomb interaction, derived from Eq. (27), is explicitly

$$V^{\mathrm{C}}_{\mathbf{G}\mathbf{G}'}(\mathbf{Q}) = V^{3D}_{\mathbf{G}\mathbf{G}'}(\mathbf{Q}) - p_{G_z}p_{G'_z}\frac{4\pi(1-e^{-|\mathbf{Q}+\mathbf{G}_\parallel|L})}{|\mathbf{Q}+\mathbf{G}_\parallel|L} \times \frac{|\mathbf{Q}+\mathbf{G}_\parallel|^2 - G_zG'_z}{\left(|\mathbf{Q}+\mathbf{G}_\parallel|^2+G_z^2\right)\left(|\mathbf{Q}+\mathbf{G}_\parallel|^2+G_z'^2\right)}\delta_{\mathbf{G}_\parallel\mathbf{G}'_\parallel}, \quad (29)$$

where

$$V^{3D}_{\mathbf{G}\mathbf{G}'}(\mathbf{Q}) = \frac{4\pi}{|\mathbf{Q}+\mathbf{G}|^2}\delta_{\mathbf{G}\mathbf{G}'} \quad (30)$$

and $p_{G_z} = (-1)^n$, where $G_z = \frac{2\pi n}{L}$; $n = 0, \pm1, \pm2, \ldots$. Truncated Coulomb interaction (29) has a more complicated form than those proposed in Refs. [53,54], however, it is obviously more constrained (in the sense that both source (z') and potential (z) are limited in $z, z' \in [-L/2, L/2]$), which enables the use of much fewer vacuum layers in supercell calculations. Considering that χ_0 and V^{C} [the main ingredients entering in Dyson's equation (19)] satisfy equivalent Fourier expansions (22) and (28) the same Fourier expansion applies to screened Coulomb interaction W_0

$$W_0(\mathbf{r},\mathbf{r}',\omega) = \frac{1}{L}\sum_{\mathbf{G}\mathbf{G}'}\int_{\mathrm{SBZ}}\frac{d\mathbf{Q}}{(2\pi)^2}e^{i(\mathbf{Q}+\mathbf{G})\mathbf{r}}e^{-i(\mathbf{Q}+\mathbf{G}')\mathbf{r}'}W^0_{\mathbf{G}\mathbf{G}'}(\mathbf{Q},\omega). \quad (31)$$

After the expansions (22), (28), and (31) are inserted in Dyson's equation (19) it converts into matrix equation

$$W^0_{\mathbf{G}\mathbf{G}'}(\mathbf{Q},\omega) = V^{\mathrm{C}}_{\mathbf{G}\mathbf{G}'}(\mathbf{Q}) + \sum_{\mathbf{G}_1\mathbf{G}_2}V^{\mathrm{C}}_{\mathbf{G}\mathbf{G}_1}(\mathbf{Q})\chi^0_{\mathbf{G}_1\mathbf{G}_2}(\mathbf{Q},\omega)W^0_{\mathbf{G}_2\mathbf{G}'}(\mathbf{Q},\omega), \quad (32)$$

where $\chi^0_{\mathbf{G}\mathbf{G}'}$ and $V^{\mathrm{C}}_{\mathbf{G}\mathbf{G}'}$ are explicit matrices (23) and (29), respectively. The solution of the equation (32) has the form

$$W^0_{\mathbf{G}\mathbf{G}'}(\mathbf{Q},\omega) = \sum_{\mathbf{G}_1}\mathcal{E}^{-1}_{\mathbf{G}\mathbf{G}_1}(\mathbf{Q},\omega)V^{\mathrm{C}}_{\mathbf{G}_1\mathbf{G}'}(\mathbf{Q}), \quad (33)$$

where the dielectric matrix is

$$\mathcal{E}_{\mathbf{G}\mathbf{G}'}(\mathbf{Q},\omega) = \delta_{\mathbf{G}\mathbf{G}'} - \sum_{\mathbf{G}_1}V^{\mathrm{C}}_{\mathbf{G}\mathbf{G}_1}(\mathbf{Q})\chi^0_{\mathbf{G}_1\mathbf{G}'}(\mathbf{Q},\omega). \quad (34)$$

Now we have all ingredients required to determine the exchange-correlation self-energy $\Sigma^{\mathrm{XC},0}$. After the Bloch wave functions and energies (21) and Fourier expansion (28) are inserted in exchange self-energy (16), it becomes

$$\Sigma^{\mathrm{X}}_{n\mathbf{K}} = -\frac{1}{L}\sum_m\int_{\mathrm{SBZ}}\frac{d\mathbf{Q}}{(2\pi)^2}f_{m\mathbf{K}+\mathbf{Q}} \times \sum_{\mathbf{G}\mathbf{G}'}\rho^*_{n\mathbf{K},m\mathbf{K}+\mathbf{Q}}(\mathbf{G})V^{\mathrm{C}}_{\mathbf{G}\mathbf{G}'}(\mathbf{Q})\rho_{n\mathbf{K},m\mathbf{K}+\mathbf{Q}}(\mathbf{G}'), \quad (35)$$

where we have also used the definition of charge vertices (24). It can be shown that if the 2D crystal possesses the center of inversion, i.e., $W_0(\mathbf{r},\mathbf{r}') = W_0(-\mathbf{r},-\mathbf{r}')$, then the propagator W_0 satisfies the following property:

$$\mathrm{Im}W_0(\mathbf{r},\mathbf{r}',\omega) = \frac{1}{L}\sum_{\mathbf{G}\mathbf{G}'}\int_{\mathrm{SBZ}}\frac{d\mathbf{Q}}{(2\pi)^2} \times e^{i(\mathbf{Q}+\mathbf{G})\mathbf{r}}e^{-i(\mathbf{Q}+\mathbf{G}')\mathbf{r}'}\mathrm{Im}W^0_{\mathbf{G}\mathbf{G}'}(\mathbf{Q},\omega). \quad (36)$$

This enables that the correlation propagator (18), according to definition (14), satisfies next Fourier expansion

$$\Gamma_0(\mathbf{r},\mathbf{r}',\omega) = \frac{1}{L}\sum_{\mathbf{G}\mathbf{G}'}\int_{\mathrm{SBZ}}\frac{d\mathbf{Q}}{(2\pi)^2} \times e^{i(\mathbf{Q}+\mathbf{G})\mathbf{r}}e^{-i(\mathbf{Q}+\mathbf{G}')\mathbf{r}'}\Gamma^0_{\mathbf{G}\mathbf{G}'}(\mathbf{Q},\omega), \quad (37)$$

where

$$\Gamma^0_{\mathbf{G}\mathbf{G}'}(\mathbf{Q},\omega) = \int_0^\infty d\omega'\frac{S^0_{\mathbf{G}\mathbf{G}'}(\mathbf{Q},\omega')}{\omega-\omega'+i\delta}, \quad (38)$$

and where the spectral matrix is

$$S^0_{\mathbf{G}\mathbf{G}'}(\mathbf{Q},\omega) = -\frac{1}{\pi}\mathrm{Im}W^0_{\mathbf{G}\mathbf{G}'}(\mathbf{Q},\omega). \quad (39)$$

Although center of inversion symmetry is not always satisfied, and especially not when 2D crystal is in interaction with the substrate (substrate screening evidently breaks the center of inversion), we will still assume that the expansion (37)–(39) is always valid. This makes the derivation of correlation self-energy $\Sigma^C_{n\mathbf{K}}(\omega)$ equivalent to derivation of exchange self-energy $\Sigma^{\mathrm{X}}_{n\mathbf{K}}$. After the Bloch wave functions and energies (21) and Fourier expansion (37) are inserted in correlation self-energy (17), it becomes

$$\Sigma^{\mathrm{C},0}_{n\mathbf{K}}(\omega) = \frac{1}{L}\sum_m\int_{\mathrm{SBZ}}\frac{d\mathbf{Q}}{(2\pi)^2}\sum_{\mathbf{G}\mathbf{G}'}\rho^*_{n\mathbf{K},m\mathbf{K}+\mathbf{Q}}(\mathbf{G})\rho_{n\mathbf{K},m\mathbf{K}+\mathbf{Q}}(\mathbf{G}') \times \left\{(1-f_{m\mathbf{K}+\mathbf{Q}})\,\Gamma^0_{\mathbf{G}\mathbf{G}'}(\mathbf{Q},\omega-E_{m\mathbf{K}+\mathbf{Q}}) - f_{m\mathbf{K}+\mathbf{Q}}\,\Gamma^0_{\mathbf{G}\mathbf{G}'}(\mathbf{Q},E_{m\mathbf{K}+\mathbf{Q}}-\omega)\right\}. \quad (40)$$

Finally, after the exchange and correlation self-energies (35) and (40) are inserted in Eq. (8) the Green's function of Bloch state $|n,\mathbf{K}\rangle$ is

$$G_{n\mathbf{K}}(\omega) = \frac{1}{\omega - E_{n\mathbf{K}} + E^{\mathrm{XC}}_{n\mathbf{K}} - \Sigma^{\mathrm{X}}_{n\mathbf{K}} - \Sigma^{\mathrm{C},0}_{n\mathbf{K}}(\omega)}, \quad (41)$$

where in KS energy $E_{n\mathbf{K}}$ the DFT exchange-correlation contribution $E^{\mathrm{XC}}_{n\mathbf{K}}$ is extracted, to avoid double counting. In next sections we will describe the derivation of the correlation self-energy induced by proximity of substrate crystal $\Delta\Sigma^{\mathrm{C,S}}_{n\mathbf{K}}$.

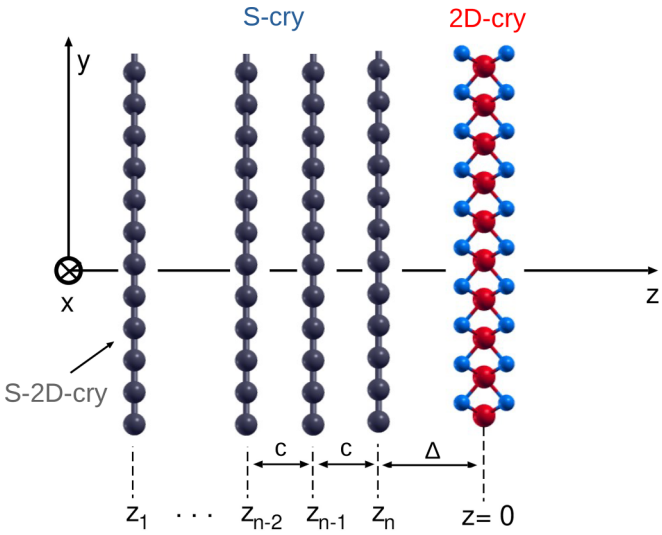

FIG. 2. The 2D-CRY centered in $z = 0$ plane is physisorbed at S-CRY consisting of n S-2D-CRYs occupying $z_1 = -\Delta - (n-1)c, \ldots, z_{n-1} = -\Delta - c, z_n = -\Delta$ planes.

C. G_0W_S approximation applied to calculate the Green's function of quantum state $|n, \mathbf{K}\rangle$ in supported 2D crystal

Very often a 2D crystal is physisorbed on substrate crystal, which can be a van der Waals heterostructure of several 2D crystals, as illustrated in Fig. 2. For simplicity, from now on, the 2D crystal whose quasiparticle (QP) properties is calculated is abbreviated as 2D-CRY and supporting crystal or substrate is abbreviated as S-CRY. We also suppose that S-CRY is homogeneous van der Waals heterostructure consisting of equal elementary blocks (substrate 2D crystal) we abbreviate as S-2D-CRY. The 2D-CRY is centered in $z = 0$ plane and S-CRY is composed of n S-2D-CRYs occupying $z_1 = -\Delta - (n-1)c, \ldots, z_{n-1} = -\Delta - c, z_n = -\Delta$ planes, as illustrated in Fig. 2. We assume that the chemical bonding between 2D-CRY and S-CRY has vdW character, so that the orbital hybridization between the two crystals is neglected. Therefore the S-CRY and 2D-CRY are here considered as two chemically independent crystals, which interact only via long-range Coulomb interaction. More specifically, when the S-CRY is brought close to 2D-CRY then it causes next modification of screened Coulomb interaction in 2D-CRY

$$W_0 \rightarrow W_S, \tag{42}$$

where the renormalized propagator W_S satisfies the following Dyson's equation:

$$W_S(\mathbf{r}, \mathbf{r}', \omega) = V_S(\mathbf{r}, \mathbf{r}') + \int d\mathbf{r}_1 d\mathbf{r}_2 V_S(\mathbf{r}, \mathbf{r}_1)\chi_0(\mathbf{r}_1, \mathbf{r}_2, \omega)W_S(\mathbf{r}_2, \mathbf{r}', \omega). \tag{43}$$

The Dyson's equation (43) is basically equal to Eq. (19) with the only difference that bare propagator V must be replaced with the substrate screened propagator

$$V_S(\mathbf{r}, \mathbf{r}', \omega) = V(\mathbf{r}, \mathbf{r}') + \Delta V(\mathbf{r}, \mathbf{r}', \omega), \tag{44}$$

where the substrate polarization effects are included in the induced propagator $\Delta V(\mathbf{r}, \mathbf{r}', \omega)$. If we suppose that S-CRY is homogeneous in x-y plane, then the substrate screened propagator can be Fourier transformed as

$$V_S(\mathbf{r}, \mathbf{r}', \omega) = \int \frac{d\mathbf{Q}}{(2\pi)^2} e^{i\mathbf{Q}(\boldsymbol{\rho}-\boldsymbol{\rho}')} V_S(\mathbf{Q}, \omega, z, z') \tag{45}$$

so that it satisfies next Dyson's equation

$$V_S(\mathbf{Q}, \omega, z, z') = V(\mathbf{Q}, z, z') + \int dz_1 dz_2 V(\mathbf{Q}, z, z_1)\chi_0^S \times (\mathbf{Q}, \omega, z_1, z_2)V_S(\mathbf{Q}, \omega, z_2, z'), \tag{46}$$

where χ_0^S is S-CRY irreducible polarizability. If the overlap between electronic orbitals in the neighboring S-2D-CRYs (in S-CRY) is negligible then it means that irreducible polarizabilities of individual S-2D-CRYs (elementary building block) remains almost unchanged even after S-2D-CRYs are stacked into S-CRY. Moreover if we assume that S-2D-CRYs are 2D sheets occupying $z = z_i$ planes then the irreducible polarizability of entire S-CRY can be approximated as [55]

$$\chi_0^S(\mathbf{Q}, \omega, z, z') = \chi_0^{S2D}(\mathbf{Q}, \omega) \sum_{i=1,n} \delta(z - z_i)\delta(z' - z_i). \tag{47}$$

The integrated nonlocal S-2D-CRY irreducible polarizability, also called 2D irreducible polarizability, is then

$$\chi_0^{S2D}(\mathbf{Q}, \omega) = \int_{-L_{S2D}/2}^{L_{S2D}/2} dz \int_{-L_{S2D}/2}^{L_{S2D}/2} dz' \chi_0^{S2D}(\mathbf{Q}, \omega, z, z') = L_{S2D}\chi^{0,S2D}_{\mathbf{G}=0\mathbf{G}'=0}(\mathbf{Q}, \omega), \tag{48}$$

where the irreducible polarizability matrix $\chi^{0,S2D}_{\mathbf{G}\mathbf{G}'}$ has the same form (23), except that the KS wave functions $\phi_{n\mathbf{K}}$, energies $E_{n\mathbf{K}}$, and other parameters now correspond to S-2D-CRY. For example, L_{S2D} in Eq. (48) represents the supercell parameter used in S-2D-CRY ground-state calculations. Using above assumptions the Dysons equation (46) can be converted into next matrix equation [55]

$$V_{ij}^S(\mathbf{Q}, \omega) = V_{ij}(\mathbf{Q}) + \sum_{ij=1,n} V_{ik}(\mathbf{Q})\chi_{kl}^{0,S}(\mathbf{Q}, \omega)V_{lj}^S(\mathbf{Q}, \omega), \tag{49}$$

where $V_{ij}(\mathbf{Q}, \omega) = v_Q e^{-|\mathbf{Q}||z_i - z_j|}$ propagates bare and $V_{ij}^S = V_S(\mathbf{Q}, \omega, z_i, z_j)$ propagates screened Coulomb interaction between S-2D-CRYs i and j and $\chi_{ij}^{0,S}(\mathbf{Q}, \omega) = \chi_0^{S2D}(\mathbf{Q}, \omega)\delta_{ij}$. The spatially dependent screened Coulomb propagator in the region $z, z' > -\Delta$ is then [40,45,55,56]

$$V_S(\mathbf{Q}, \omega, z, z') = V(\mathbf{Q}, \omega, z, z') + \Delta V(\mathbf{Q}, \omega, z, z') = v_Q e^{-|\mathbf{Q}||z-z'|} + \Delta V(\mathbf{Q}, \omega)e^{-|\mathbf{Q}|(z+z')}, \tag{50}$$

where the (x-y) Fourier transform of the induced potential at $z = 0$ plane is

$$\Delta V(\mathbf{Q}, \omega) = v_Q D(\mathbf{Q}, \omega)e^{-2|\mathbf{Q}|\Delta}, \tag{51}$$

and the surface excitations propagator is

$$D(\mathbf{Q}, \omega) = V_{nn}^S(\mathbf{Q}, \omega)/v_Q - 1. \tag{52}$$

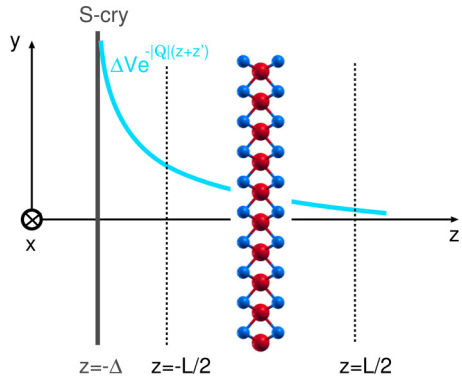

FIG. 3. The penetration of the induced potential (50) in the 2D-CRY localized in the interval $z \in [-L/2, L/2]$, where L represents the 2D-CRY unit cell in the z direction, as also illustrated in Fig. 1. The S-CRY, regardless of its thickness (number of S-2D-CRY layers n), is located in the region $z \leqslant -\Delta$, as also illustrated in Fig. 2.

It should be noted here that the induced potential ΔV in (50), also illustrated in Fig. 3, obviously violates 2D-CRY inversion symmetry. However, because its form $\Delta V \sim (2\pi/Q)e^{-2Q\Delta}2e^{-Q(z+z')}$ favors small wave vectors Q, it is mostly homogeneous potential that just weakly violates the inversion symmetry [44]. The surface excitations propagator D defines the strength of the dynamic potential, which emerges from $z = -\Delta$ surface and decreases according to the exponential law $e^{-|\mathbf{Q}|(z+z')}$, as illustrated in Fig. 3. It should be thus noted that we have broken the translation-invariant symmetry in the z direction by introducing the substrate, as the Coulomb interaction has a $z + z'$ term and not only $|z - z'|$ as before. Here we will mostly consider the case when $n = 1$, i.e., when the 2D-CRY is physisorbed at the single S-2D-CRY. In that case, solving the Dyson's equation (49) becomes trivial, so that the surface excitations propagator is

$$D(\mathbf{Q}, \omega) = \frac{1 - \epsilon_{2D}(\mathbf{Q}, \omega)}{\epsilon_{2D}(\mathbf{Q}, \omega)}, \tag{53}$$

where

$$\epsilon_{2D}(\mathbf{Q}, \omega) = 1 - v_Q \chi_0^{S2D}(\mathbf{Q}, \omega) \tag{54}$$

represents the 2D dielectric function of the S-2D-CRY. Analogously to the bare potential (25) the potential (44) still needs to be constrained to propagate interactions only within the region $z, z' \in [-L/2, L/2]$, i.e., the next transformation should be done $V_S \to V_S^C$ where

$$V_S^C(\mathbf{r}, \mathbf{r}', \omega) = \begin{cases} V_S(\mathbf{r}, \mathbf{r}', \omega); & z \text{ and } z' \in [-L/2, L/2] \\ 0; & z \text{ and/or } z' \notin [-L/2, L/2] \end{cases}. \tag{55}$$

It is easy to show that V_S^C satisfies [also according to assumption (45)] next Fourier expansion

$$V_S^C(\mathbf{r}, \mathbf{r}', \omega) = \frac{1}{L}\sum_{G_z G_z'} \int \frac{d\mathbf{Q}}{(2\pi)^2} e^{i\mathbf{Q}(\boldsymbol{\rho}-\boldsymbol{\rho}')} e^{iG_z z - iG_z' z'} V^{S,C}_{G_z G_z'}(\mathbf{Q}, \omega), \tag{56}$$

where the Fourier coefficients are

$$V^{S,C}_{G_z G_z'}(\mathbf{Q}, \omega) = \frac{1}{L}\int_{-L/2}^{L/2} dz \int_{-L/2}^{L/2} dz' e^{-iG_z z + iG_z' z'} V_S(\mathbf{Q}, \omega, z, z'). \tag{57}$$

Using (50) in (57) and then in (56) one obtains the Fourier transform of propagator V_S^C which, also rearranged to be compatible to the irreducible polarizability (22), becomes

$$V_S^C(\mathbf{r}, \mathbf{r}', \omega) = \frac{1}{L}\sum_{\mathbf{G}\mathbf{G}'} \int_{SBZ} \frac{d\mathbf{Q}}{(2\pi)^2} e^{i(\mathbf{Q}+\mathbf{G})\mathbf{r}} e^{-i(\mathbf{Q}+\mathbf{G}')\mathbf{r}'} V^{S,C}_{\mathbf{G}\mathbf{G}'}(\mathbf{Q}, \omega), \tag{58}$$

where

$$V^{S,C}_{\mathbf{G}\mathbf{G}'}(\mathbf{Q}, \omega) = V^C_{\mathbf{G}\mathbf{G}'}(\mathbf{Q}) + \Delta V^C_{\mathbf{G}\mathbf{G}'}(\mathbf{Q}, \omega), \tag{59}$$

the matrix of truncated induced propagator is

$$\Delta V^C_{\mathbf{G}\mathbf{G}'}(\mathbf{Q}, \omega) = \Delta V(\mathbf{Q} + \mathbf{G}_\parallel, \omega) F_{G_z}(\mathbf{Q} + \mathbf{G}_\parallel) F^*_{G_z'}(\mathbf{Q} + \mathbf{G}_\parallel) \delta_{\mathbf{G}_\parallel \mathbf{G}_\parallel'}, \tag{60}$$

and the form factors are

$$F_{G_z}(\mathbf{Q}) = \frac{2p_{G_z}}{\sqrt{L}} \frac{\mathrm{sh}(|\mathbf{Q}|L/2)}{|\mathbf{Q}| + iG_z}. \tag{61}$$

The matrix of truncated bare propagator $V^C_{\mathbf{G}\mathbf{G}'}$ is given by Eq. (29). The substrate screened propagator (58)–(61) is constrained to propagate the Coulomb interaction in the region $z, z' \in [-L/2, L/2]$, but in the absence of 2D-CRY. After the 2D-CRY is introduced, the total screened Coulomb interaction can be derived by solving Dyson's equation (43) whose solution, in the matrix representation, is

$$W^S_{\mathbf{G}\mathbf{G}'}(\mathbf{Q}, \omega) = \sum_{\mathbf{G}_1} [\mathcal{E}^S(\mathbf{Q}, \omega)]^{-1}_{\mathbf{G}\mathbf{G}_1} V^{S,C}_{\mathbf{G}_1\mathbf{G}'}(\mathbf{Q}), \tag{62}$$

where the dielectric matrix in 2D-CRY, now modified due to the presence of nearby S-CRY, is

$$\mathcal{E}^S_{\mathbf{G}\mathbf{G}'}(\mathbf{Q}, \omega) = \delta_{\mathbf{G}\mathbf{G}'} - \sum_{\mathbf{G}_1} V^{S,C}_{\mathbf{G}\mathbf{G}_1}(\mathbf{Q}) \chi^0_{\mathbf{G}_1\mathbf{G}'}(\mathbf{Q}, \omega). \tag{63}$$

It should be emphasized that the propagator (62) represents the potential between test charges in the constrained region $z, z' \in [-L/2, L/2]$, also including the polarization of the S-CRY. Once the matrix $W^S_{\mathbf{G}\mathbf{G}'}$ is derived, the derivation of the correlation self-energy $\Sigma^{C,S}$ becomes analogous to derivation of bare self-energy $\Sigma^{C,0}$, as described in Sec. II B. According to Eqs. (38)–(40) and modification (42) the correlation self-energy in supported 2D-CRY becomes

$$\Sigma^{C,S}_{n\mathbf{K}}(\omega) = \frac{1}{L}\sum_m \int_{SBZ} \frac{d\mathbf{Q}}{(2\pi)^2} \sum_{\mathbf{G}\mathbf{G}'} \rho^*_{n\mathbf{K}, m\mathbf{K}+\mathbf{Q}}(\mathbf{G}) \rho_{n\mathbf{K}, m\mathbf{K}+\mathbf{Q}}(\mathbf{G}') \times \left\{ (1 - f_{m\mathbf{K}+\mathbf{Q}})\, \Gamma^S_{\mathbf{G}\mathbf{G}'}(\mathbf{Q}, \omega - E_{m\mathbf{K}+\mathbf{Q}}) - f_{m\mathbf{K}+\mathbf{Q}}\, \Gamma^S_{\mathbf{G}\mathbf{G}'}(\mathbf{Q}, E_{m\mathbf{K}+\mathbf{Q}} - \omega) \right\}, \tag{64}$$

where

$$\Gamma^{\mathrm{S}}_{\mathbf{GG}'}(\mathbf{Q},\omega)=\int_0^\infty d\omega'\frac{S^{\mathrm{S}}_{\mathbf{GG}'}(\mathbf{Q},\omega')}{\omega-\omega'+i\delta}, \tag{65}$$

and the spectrum of electronic excitations in 2D-CRY, including the polarization of S-CRY, is

$$S^{\mathrm{S}}_{\mathbf{GG}'}(\mathbf{Q},\omega)=-\frac{1}{\pi}\mathrm{Im}W^{\mathrm{S}}_{\mathbf{GG}'}(\mathbf{Q},\omega). \tag{66}$$

From the definitions (43)–(44) it is obvious that W_{S} can be divided to bare and induced contributions $W_{\mathrm{S}}=V^{\mathrm{C}}+\Delta W_{\mathrm{S}}$, which means that the exchange self-energy $\Sigma^{\mathrm{X}}_{n\mathbf{K}}$ remains unchanged and is given by Eq. (35). The Green's function of Bloch state $|n,\mathbf{K}\rangle$ in 2D-CRY supported by S-CRY is then

$$G_{n\mathbf{K}}(\omega)=\frac{1}{\omega-E_{n\mathbf{K}}+E^{\mathrm{XC}}_{n\mathbf{K}}-\Sigma^{\mathrm{XC,S}}_{n\mathbf{K}}(\omega)}, \tag{67}$$

where

$$\Sigma^{\mathrm{XC,S}}_{n\mathbf{K}}(\omega)=\Sigma^{\mathrm{X}}_{n\mathbf{K}}+\Sigma^{\mathrm{C,S}}_{n\mathbf{K}}(\omega). \tag{68}$$

Very similar *GW* procedure was used to study the molecular electronic levels shifts induced by different solvents using polarizable continuum model (PCM) [57–59], or energy levels and photoluminescence in various defects in hexagonal boron nitride using many-body finite-size cluster *GW*-BSE approach [60,61]. The main idea there is division into subsystems (e.g., solution, system 1 and solvent, system 2) and neglecting the overlap between subsystems. Then the screened Coulomb interaction W (entering the *GW*-BSE scheme), which accounts the polarizability of both subsystems is simple $W=\tilde{v}+\tilde{v}\chi_0^1 W$ and $\tilde{v}=v+v\chi_0^2\tilde{v}$, where $\chi_0^{1,2}$ are subsystems irreducible polarizabilities and v is bare Coulomb potential. Exactly the same idea in modeling W^{S} is used here, see, for example, Eq. (43) and Eq. (49), where our subsystems 1 and 2 are 2D-CRY and S-CRY, respectively. Moreover, very similar derivation of the screened interaction W, including the division into two nonoverlapping polarizabilities $\chi_0^{1,2}$, was proposed in order to solve the Bethe-Salpeter equation (using significantly reduced computer resources) in molecule/substrate [62] or in various 2D vdW heterostructures [63].

D. $G_0\Delta W_{\mathrm{S}}$ approximation

So far we have considered the total exchange-correlation self-energy in 2D-CRY supported by S-CRY. The total in the sense that it consists of bare (intrinsic) self-energy $\Sigma^{\mathrm{XC},0}$ plus induced self-energy $\Delta\Sigma^{\mathrm{C,S}}$ caused by the presence of supporting crystals. However, because the $\Sigma^{\mathrm{XC},0}$ can be calculated very accurately using many existing *ab initio* packages the real advantage of the above method is determination of induced correlation self-energy

$$\begin{aligned}\Delta\Sigma^{\mathrm{C,S}}_{n\mathbf{K}}(\omega)&=\Sigma^{\mathrm{XC,S}}_{n\mathbf{K}}(\omega)-\Sigma^{\mathrm{XC},0}_{n\mathbf{K}}(\omega)\\&=\Sigma^{\mathrm{C,S}}_{n\mathbf{K}}(\omega)-\Sigma^{\mathrm{C},0}_{n\mathbf{K}}(\omega).\end{aligned} \tag{69}$$

Because in both cases the Σ^{X} contributions are equal they cancel, which enables bypassing the calculation of computationally demanding exchange self-energy (35). After using (40) and (64) in (69) we get

$$\begin{aligned}\Delta\Sigma^{\mathrm{C,S}}_{n\mathbf{K}}(\omega)=\frac{1}{L}\sum_m\int_{\mathrm{SBZ}}\frac{d\mathbf{Q}}{(2\pi)^2}\sum_{\mathbf{GG}'}\rho^*_{n\mathbf{K},m\mathbf{K}+\mathbf{Q}}(\mathbf{G})\rho_{n\mathbf{K},m\mathbf{K}+\mathbf{Q}}(\mathbf{G}')\\\times\big\{(1-f_{m\mathbf{K}+\mathbf{Q}})\,\Delta\Gamma^{\mathrm{S}}_{\mathbf{GG}'}(\mathbf{Q},\omega-E_{m\mathbf{K}+\mathbf{Q}})\\-f_{m\mathbf{K}+\mathbf{Q}}\,\Delta\Gamma^{\mathrm{S}}_{\mathbf{GG}'}(\mathbf{Q},E_{m\mathbf{K}+\mathbf{Q}}-\omega)\big\},\end{aligned} \tag{70}$$

where

$$\Delta\Gamma^{\mathrm{S}}_{\mathbf{GG}'}(\mathbf{Q},\omega)=\int_0^\infty d\omega'\frac{\Delta S^{\mathrm{S}}_{\mathbf{GG}'}(\mathbf{Q},\omega')}{\omega-\omega'+i\delta}. \tag{71}$$

The spectrum of electronic excitations induced by presence of S-CRY is then

$$\Delta S^{\mathrm{S}}_{\mathbf{GG}'}(\mathbf{Q},\omega)=-\frac{1}{\pi}\mathrm{Im}\Delta W^{\mathrm{S}}_{\mathbf{GG}'}(\mathbf{Q},\omega), \tag{72}$$

where

$$\Delta W^{\mathrm{S}}_{\mathbf{GG}'}(\mathbf{Q},\omega)=W^{\mathrm{S}}_{\mathbf{GG}'}(\mathbf{Q},\omega)-W^{0}_{\mathbf{GG}'}(\mathbf{Q},\omega). \tag{73}$$

So, the only values, which essentially need to be calculated, are screened Coulomb interactions in self-standing and in supported 2D-CRY, i.e., W_0 and W_{S}, respectively. Here we calculate the full frequency-dependent induced correlation self-energy $\Delta\Sigma^{\mathrm{C,S}}$ exactly according to the formulas Eqs. (70)–(73). The static Coulomb-hole plus screened exchange (COHSEX) approximation [47] will be used only for the calculation of self-energy of point (test) charge, in Sec. IV. Finally, the total exchange-correlation self-energy can be, using Eq. (69), determined as

$$\Sigma^{\mathrm{XC,S}}_{n\mathbf{K}}(\omega)=\Sigma^{\mathrm{XC},0}_{n\mathbf{K}}(\omega)+\Delta\Sigma^{\mathrm{C,S}}_{n\mathbf{K}}(\omega), \tag{74}$$

where $\Sigma^{\mathrm{XC},0}$ can be obtained, for example, using some of the existing *ab initio* packages. According to (67) and (74) the Green's function of an electron or hole in quantum state $|n,\mathbf{K}\rangle$ in G_0W_{S} approximation is

$$G_{n\mathbf{K}}(\omega)=\frac{1}{\omega-E_{n\mathbf{K}}+E^{\mathrm{XC}}_{n\mathbf{K}}-\Sigma^{\mathrm{XC},0}_{n\mathbf{K}}(\omega)-\Delta\Sigma^{\mathrm{C,S}}_{n\mathbf{K}}(\omega)}. \tag{75}$$

In this paper we will use two approximations. The first approximation is

$$\Sigma^{\mathrm{XC},0}_{n\mathbf{K}}(\omega)\approx E^{\mathrm{XC}}_{n\mathbf{K}}. \tag{76}$$

In this approximation, which does not include intrinsic self-energy corrections, the DFT energies $E_{n\mathbf{K}}$ are used to calculate the irreducible polarizability (23) and thus the induced self-energy $\Delta\Sigma^{\mathrm{C,S}}$. In the second approximation

$$\Sigma^{\mathrm{XC},0}_{n\mathbf{K}}(\omega)\approx\begin{cases}E^{\mathrm{XC}}_{n\mathbf{K}}-\Delta_{\mathrm{g}}/2; & E_{n\mathbf{K}}<E_{\mathrm{F}}\\ E^{\mathrm{XC}}_{n\mathbf{K}}+\Delta_{\mathrm{g}}/2; & E_{n\mathbf{K}}>E_{\mathrm{F}}\end{cases}, \tag{77}$$

where Δ_{g} is rigid energy shift set to satisfy the G_0W_0 or experimental band gap, and E_{F} is Fermi energy. In this approximation the corrected energies $E_{n\mathbf{K}}\pm\Delta_{\mathrm{g}}/2$ are used to calculate the irreducible polarizability (23) and thus the induced self-energy $\Delta\Sigma^{\mathrm{C,S}}$. Of course, it would be better instead of using the approximations (76) and (77) in Eq. (75) to insert the exact $\Sigma^{XC,0}$ derived by formula Eq. (40). However, we have noticed that the energy shifts $\Delta E_{\mathrm{C,V,g}}$ significantly depend on which quasiparticle energies $\tilde{E}_{n\mathbf{K}}$ are inserted in 2D-CRY irreducible polarizability (23), or better said, on

which initial QP energies $\tilde{E}_{n\mathbf{K}}$ were used in the calculation of the screened Coulomb interaction (62). To put it even more simply; the energy shifts $\Delta E_{\mathrm{C,V,g}}$ are very sensitive to which band gap E_{g} we use to calculate W^{S} but they are not so sensitive to the details of energy bands $\tilde{E}_{n\mathbf{K}}$ along the Brillouin zone, so that the scissor operator (77) is the most efficient approximation. More specifically; suppose that Hamiltonian representing the electron-electron interaction is split to intracontribution (representing the interaction of electrons within 2D-CRY) and intercontribution (representing the interaction between the electrons in 2D-CRY and electrons in S-CRY). Since there is no electronic overlap between 2D-CRY and S-CRY, this division is exact. Suppose that intraelectron-electron interaction is a part of the unperturbed Hamiltonian H_0, and that interelectron-electron interaction represents perturbation. Moreover, suppose that we force H_0 to be single-particle (bilinear) operator, as in Eq. (1), which can be diagonalized. This means that all intraelectron-electron interaction is stored in unperturbed QP energies and wave functions from which new Green's functions G_1 can be constructed. This is of course not exact but also not a bad approximation if the QP approximation is satisfied (which is the case for the 2D semiconductors). Then according the many-body perturbation theory the induced self-energy $\Delta\Sigma^{\mathrm{C,S}}_{n\mathbf{K}}$ is given by exactly the same formula Eq. (70) but in which enters new Green's function G_1. Therefore, if in $\Delta\Sigma^{\mathrm{C,S}}_{n\mathbf{K}}$ we use Green's function G_0, it means that all intraelectron-electron interaction is stored in KS energies and this corresponds to approximation Eq. (76), and if we use G_1, it means that all intraelectron-electron interaction is stored in G_0W_0 QP energies $\tilde{E}_{n\mathbf{K}}$ and it corresponds to aproximation Eq. (77). If we choose this second option, it implies a calculation of $\Sigma^{\mathrm{XC},0}$ for all wave vectors $\mathbf{K}$ and bands n, which is computationally extremely demanding and perhaps unnecessary. So this is the reason why here we use the scissor operator approximation Eq. (77). Using (76) or standard G_0W_0 $\Sigma^{\mathrm{XC},0}$ in (75), because then only the Green's function G_0 are used in W^{S}, provide identical shifts $\Delta E_{\mathrm{C,V,g}}$. However, the approximation (77), because then an already corrected energies are used in both G_1 and in screened propagator W^{S}_1, represents a kind of $G_1\Delta W^{\mathrm{S}}_1$ approximation so that it provides significantly more accurate shifts $\Delta E_{\mathrm{C,V,g}}$. Although it is not a $G_1\Delta W^{\mathrm{S}}_1$ approximation entirely, because in G_1 and ΔW^{S}_1 the only energies are updated, but not the wave functions.

The electron/hole line shape of Bloch state $|n\mathbf{K}\rangle$ is then defined by next spectral function

$$A_{n\mathbf{K}}(\omega) = -\frac{1}{\pi}\frac{\mathrm{Im}\Delta\Sigma^{\mathrm{C,S}}_{n\mathbf{K}}(\omega)}{\left[\omega-\tilde{E}_{n\mathbf{K}}-\mathrm{Re}\Delta\Sigma^{\mathrm{C,S}}_{n\mathbf{K}}(\omega)\right]^2+\left[\mathrm{Im}\Delta\Sigma^{\mathrm{C,S}}_{n\mathbf{K}}(\omega)\right]^2}, \tag{78}$$

where $\tilde{E}_{n\mathbf{K}}=E_{n\mathbf{K}}$ in first, and $\tilde{E}_{n\mathbf{K}}=E_{n\mathbf{K}}\pm\Delta_{\mathrm{g}}/2$ in second approximation. The energy shift of Bloch state $|n\mathbf{K}\rangle$, caused by S-CRY, will be determined from the position of the main peak in the spectral function (78) relative to the energy $\tilde{E}_{n\mathbf{K}}$. The imaginary part of the induced self-energy $\mathrm{Im}\Delta\Sigma^{\mathrm{C,S}}$ determines the decay rate of the Bloch state $|n\mathbf{K}\rangle$ or, for this paper more important, the plasmonic satellites in the spectrum, induced by nearby graphene.

Here it is also important to note that a very similar $G\Delta W$ method was used to calculate the band gap in $MoSe_2$/Gr-BL composite [26]. There in order to include graphene polarization effects, the $MoSe_2$ polarizability is corrected by adding the graphene polarizability $\chi^{0,\mathrm{MoSe_2}}\rightarrow\chi^{0,\mathrm{MoSe_2}}+\chi^{0,\mathrm{bilayer}}$, which is also mapped to $MoSe_2$ unit cell. On the other hand, we correct the bare Coulomb interaction V^{C} (propagating the interactions within TMD unit cell) by the induced graphene Coulomb interaction ΔV^{C} penetrating the TMD unit cell [see Eq. (59)]. In Ref. [26] the CLFE are excluded in the parallel direction in the $\chi^{0,\mathrm{bilayer}}$, and we exclude them in the ΔV^{C} potential. However, we also exclude the CLFE in χ^{S}_0 in all three directions [see Eq. (47)], which make the method developed in Ref. [26] superior. The advantage of our method is that potential ΔW^S spreads only within the TMD unit cell, while the inverted dielectric function $\Delta\epsilon^{-1}$ in Ref. [26] spreads throughout the entire graphene/$MoSe_2$ supercell. This allows the dimension of the matrices, in $\mathbf{G}$ space, to be significantly smaller in our case.

III. COMPUTATIONAL DETAILS

The ground-state wave functions $\phi_{n\mathbf{K}}$ and energies $E_{n\mathbf{K}}$ of 2D crystals WS_2, MoS_2, graphene, and hBN (above named 2D-CRY or S-2D-CRY) were calculated using a plane-wave self-consistent field DFT code (PWSCF) within the QUANTUM ESPRESSO (QE) package [64]. For all four 2D crystals the core-electrons interaction was approximated by the standard Martins-Troulier norm-conserving pseudopotential where semicore electrons are treated as valence electrons [65,66] and the exchange correlation (XC) potentials were approximated by the scalar-relativistic Perdew-Burke-Ernzerhof (PBE) generalized gradient approximation (GGA) functional [67]. The Bravais lattices of all 2D crystals are hexagonal, where the experimental unit cells $a=3.19$ Å, $a=3.16$ Å, $a=2.46$ Å, and $a=2.51$ Å for WS_2, MoS_2, graphene, and hBN, respectively, are used. The superlattice constants are $L=5a$ for all four crystals. Because of similar unit cells a, the ground-state electronic densities were calculated by using the same $12\times12\times1$ Monkhorst-Pack K meshes [68] and the plane-wave cutoff energy was 50 Ry. During the calculation of the RPA irreducible polarizabilities (23) in WS_2, MoS_2, and hBN the crystal local field effects are included only in z direction [i.e., $\mathbf{G}=(\mathbf{G}_{\parallel}=0,G_z)$], where used cutoff energy was $E_{\mathrm{cut}}=20$ Ry. The wave vector ($\mathbf{K}$) summations were performed by using the $51\times51\times1$ K mesh and the bands (n,m) summations were performed over 40, 50, and 30 bands in WS_2, MoS_2, and hBN, respectively. The same number of bands is used in the calculation of the induced self-energy Eq. (70). Although the standard G_0W_0 method requires a much larger number of unoccupied bands it is not the case for the $G_0\Delta W_S$ method. Namely, the induced Coulomb potential ΔW_S in the 2D-CRY region changes more slowly than the intrinsic potential W_0, so that the matrix elements [ρ's in (70)] representing the transitions between Bloch states, decrease rapidly for transitions to higher bands. The 2D irreducible polarizabilities (48) of the S-2D-CRYs (graphene and hBN) are determined using $\mathbf{G}=0,\mathbf{G}'=0$ component of RPA irreducible polarizabilities (23). The band summations were performed over 20 and 30 bands, for graphene and

TABLE I. The band gap shifts $-\Delta E_g$ in WS_2 caused by the vicinity of various S-CRYs (listed in the first row). (second row) The simulated $-\Delta E_g$ obtained using first approximation Eq. (76), i.e. relative to DFT band gap $E_{g(DFT)} = 1.82\,eV$ in self-standing WS_2. (third row) The simulated $-\Delta E_g$ obtained using second approximation [Eq. (77)], i.e., relative to the experimental band gap $E_g = 2.4\,eV$ in WS_2/SiO_2. (fourth row) Theoretical $-\Delta E_g$ relative to the theoretical band gap $E_{g(GW)} = 2.38\,eV$ [18] in WS_2/SiO_2. (fifth row) The experimental $-\Delta E_g$ relative to experimental band gap $E_{g(EXPT)} = 2.4\,eV$ in WS_2/SiO_2 [18] and relative to band gaps in WS_2/hBN-∞ [23,24].

$-\Delta E_g$[meV] in WS_2/S-CRY					
S-CRY	Gr-SL	Gr-BL	Gr-TL	Gr-∞	hBN-∞
App. 1 [Eq. (76)]	103	124	124	124	
App. 2 [Eq. (77)]	147	151	152	152	51
Theor.	170 [18]	195 [18]	205 [18]		
Expt.	60 [23]	135 [18]	150 [18]	140 [24]	
	140 [18]				

hBN, respectively. The graphenes are pristine or doped by electrons, where chosen concentrations of injected electrons are $n = 10^{13}\,cm^{-2}$, $n = 10^{14}\,cm^{-2}$, or $n = 1.76 \times 10^{14}\,cm^{-2}$, per graphene layer. The inclusion of graphene doping does not change the proposed formalism. The doping effects are included at the level of the self-consistent ground-state calculation; the extra electrons (of concentrations n) are injected into the graphene unit cell and then the electronic degrees of freedom are relaxed. The obtained KS states are then used in exactly the same expression Eq. (23) to calculate the graphene irreducible polarizability with very large precision, so that the wave vector ($\mathbf{K}$) summations were performed by using $201 \times 201 \times 1$ K mesh. This large precision is necessary in order to include as accurately as possible the contribution of intraband ($\pi^* \to \pi^*$) and interband ($\pi \to \pi^*$) electron-hole excitations in the vicinity of the Dirac point. This finally influences the accuracy of the calculation (the intensity and dispersion relation) of Dirac plasmon, and thus, here the most relevant, the Dirac plasmaron that appears in the quasiparticle spectrum. The gr-gr or hBN-hBN distances are fixed to $c = 3.3$ Å, as in natural graphite or in bulk hBN [69,70]. The separation between topmost graphene or hBN (in S-CRY) and closer sulfur plane (in WS_2 or in MoS_2) is fixed to 3.0 Å, so that $\Delta = 4.6$ Å in both cases. If 2D-CRY is hBN, the separation between topmost graphene and hBN is fixed to $\Delta = 3.0$ Å. Small variation of parameter Δ, e.g., of about ± 0.1 Å, causes negligible shifts $\Delta E_{C,V,g}$ of just several meV, which is less than the numerical accuracy in this calculation. This is the reason why here we do not vary parameter Δ.

IV. RESULTS AND DISCUSSION

In order to test the accuracy of the derived theory, in Sec. IV A we compare the results for the change of the band gap $-\Delta E_g$ in WS_2, MoS_2, and hBN physisorbed on various substrates, with recent experimental and theoretical results. Also, we will discuss why the polarization shifts are smaller in TMDs than in hBN. In Sec. IV B we compare the band-shifts in different points of the Brillouin zone. Finally, in Sec. IV C we discuss the effect of graphene doping on the π satellite and the D plasmaron appearing in hBN quasiparticle spectra ($-\mathrm{Im}G_{n\mathbf{K}}$) along the Γ-M-K-Γ path in the Brillouin zone, for two graphene dopings ($n = 0$ and $n > 10^{14}$). In order to check the impact of inversion symmetry violation we calculated the shifts $\Delta E_{V,C,g}$ in the 2D-CRY, which is exactly in the middle between two identical S-CRYs (recovering the inversion symmetry). The obtained shifts are exactly two times larger than those we get when we remove one S-CRY. This undoubtedly proves that the presented formulation tolerates the inversion symmetry violation.

A. Substrate-induced band gap shifts $-\Delta E_g$ in WS_2, MoS_2, and hBN SLs

WS_2. The second row in Table I shows the change of band gap $-\Delta E_g$ in WS_2 caused by adjacent Gr-SL, gr-BL, gr-TL, gr-∞, and hBN-∞ denoted in first row. Here, SL represents a single layer ($n = 1$), BL is a bilayer ($n = 2$), TL is a trilayer ($n = 3$), and ∞ signifies that S-CRY is a semi-infinite substrate ($n = \infty$). Shifts $-\Delta E_g$ were calculated based on the shifts of the valence and conduction bands (at the K point) calculated using, what we called, the first approximation [see Eq. (76)]. In other words, $-\Delta E_g$ is band gap shift relative to the DFT band gap in WS_2 $E_{g(DFT)} = 1.82\,eV$. We notice that $-\Delta E_g$ saturates very quickly with the increase of graphene layers n. This is because the already single-layer graphene provides very efficient metallic screening so that adding new layers (behind the first, the closest one) represents a negligible effect. The third row shows the same as second, but here $-\Delta E_g$ were calculated based on the shifts of the valence and conduction bands calculated using, what we called, the second approximation [see Eq. (77)]. More precisely, here $-\Delta E_g$ is band gap shift relative to the experimental band gap $E_{g(EXP)} = 2.4\,eV$ for WS_2 at SiO_2 surface, i.e., here is chosen $\Delta_g = 0.58\,eV$. The larger band gap reduces the WS_2 polarizability (its polarization becomes more rigid), which results that the polarization of S-CRY have a stronger (more direct) impact to 2D-CRY quasiparticle properties causing an additional reduction of the band gap, by about 50 meV. The fourth row shows $-\Delta E_g$ obtained using quantum electrostatic heterostructure (QEH) approach [18], relative to $E_{g(GW)} = 2.38\,eV$, obtained using G_0W_0 method. We notice that our results slightly underestimate the theoretical results taken from Ref. [18]. However, the agreement with the various experimental results listed in the fifth row of Table I is satisfactorily good. We will see later that doped graphene further reduces the band gap, which brings the result even closer to the experimental values. The last column shows the $-\Delta E_g$ in WS_2 caused by hBN-∞ surface, also relative to the experimental band gap

TABLE II. The band gap shifts $-\Delta E_g$ in MoS_2 caused by vicinity of various S-CRYs (listed in first row). (second row) The simulated $-\Delta E_g$ obtained using first approximation [Eq. (76)], i.e., relative to DFT band gap $E_{g(DFT)} = 1.81$ eV. (third row) The simulated $-\Delta E_g$ obtained using second approximation [Eq. (77)], i.e., relative to G_0W_0 band gap $E_{g(GW)} = 2.75$ eV [28]. (fourth row) Theoretical $-\Delta E_g$ relative to the *GW* band gaps $E_{g(GW)} = 2.68$ eV [27] and $E_{g(GW)} = 2.75$ eV [28]. (fifth row) The experimental $-\Delta E_g$ relative to *GW* band gap $E_{g(GW)} = 2.6$ eV [31]. All band gaps E_g refer to self-standing MoS_2.

	$-\Delta E_g$[meV] in MoS_2/S-CRY				
S-CRY	Gr-SL	Gr-BL	Gr-TL	Gr-∞	hBN-∞
App. 1 [Eq. (76)]	101	109	109	109	
App. 2 [Eq. (77)]	150	153	153	153	53
Theor.	350 [28]	390 [28]	400 [28]	540 [28]	180 [27]
					50 [28]
Expt.	70 [71]			200 [15]	140 [2]
	400 [72]			450 [25]	160 [29]

$E_{g(EXP)} = 2.4$ eV in WS_2/SiO_2. It can be seen that the hBN-∞ surface, as expected, affects the band gap significantly less than graphenes. The spectroscopic measurements in Ref. [18] and in Refs. [23,24] are performed at $T = 70$ K and at room temperature, respectively, in ultrahigh vacuum.

MoS_2. The second and third rows in Table II show the $-\Delta E_g$ in MoS_2 caused by adjacent Gr-SL, gr-BL, gr-TL, gr-∞, and hBN-∞. Similar to Table I, the $-\Delta E_g$ in second row is calculated using first approximation, i.e., relative to DFT band gap $E_{g(DFT)} = 1.81$ eV, while in third row using second approximation, i.e., relative to G_0W_0 band gap $E_{g(GW)} = 2.75$ eV, i.e., $\Delta_g = 0.94$ eV was used. Very similar to WS_2, larger band gap reduces the MoS_2 polarizability and thus allows the S-CRY to have more direct impact on 2D-CRY quasiparticle properties, resulting in 50 meV reduction of the band gap in the third row. Also, $-\Delta E_g$ saturates very quickly with the increase of graphene layers. The fourth row shows the theoretical results taken from Ref. [28] where $-\Delta E_g$ are calculated relative to G_0W_0 band gap $E_{g(GW)} = 2.75$ eV in self-standing MoS_2. One can notice that our results significantly underestimate these theoretical results, even about three times. It is possible that effects of overlap between graphene and MoS_2 orbitals, which we do not include here but are included in Ref. [28], significantly increases the band gap reduction. The above could be the truth if the covalent bond between the 2D crystals would be the case, however, here the 2D crystals are bound by a vdW chemical bond, which is the result of a long-range fluctuation-fluctuation interaction. However, precisely that long-range interaction is considered in this $G_0\Delta W_S$ method. In other words, this band gap reduction $-\Delta E_g$ (or more precisely, the entire band structure correction) provides the vdW attraction between 2D-CRY and 2D-CRY and can replace the huge cell calculations using vdW functionals. Hence, the incorporation of orbital overlap effects is expected to have no influence on $-\Delta E_g$. Moreover, some experimental results as well as comparisons with $-\Delta E_g$ in other 2D crystals support above explanation. The fifth row shows some experimental results for $-\Delta E_g$ relative to G_0W_0 band gap $E_{g(GW)} = 2.6$ eV in self-standing MoS_2. The band gap value is taken to be 2.6 eV [31] because it is the latest and, in our opinion, the most accurately calculated band gap in self-standing MoS_2 [31], which is finally confirmed by other recent calculations [27]. Taking $E_{g(GW)} = 2.6$ eV as a reference, a minor $-\Delta E_g = 70$ meV is measured in MoS_2/graphene/Ir(111) heterostructure [71], while $-\Delta E_g = 200$ meV is measured in MoS_2 on graphite substrate [15]. However, there are also results that significantly overestimate these values, for example $-\Delta E_g = 400$ meV in MoS_2/Gr-SL [72] or $-\Delta E_g = 450$ meV in MoS_2/Gr-∞ [25]. Finally, there is no reason why the $-\Delta E_g$ in MoS_2 would be even three times larger than in the isoelectronic WS_2, see fifth row in Table I. Moreover, the similarly small $-\Delta E_g = 80$ meV is measured in $MoSe_2$/Gr-BL composite [26]. We will show later that doped graphene, the same as in WS_2, increases $-\Delta E_g$ for an additional 50 meV. Also, as in WS_2 the hBN substrate (third row, last column in Table II) negligibly affects the MoS_2 band gap. The results of other theoretical and experimental investigations for $-\Delta E_g$ in MoS_2/hBN-∞ are shown in fourth and fifth row. The obtained $-\Delta E_g$ of even more than 150 meV are probably overestimated considering that hBN is, opposite to graphite, a rigid insulator. Similar to graphene, the gap changes negligibly as the number of hBN layers increases. This contradicts the results of sophisticated *GW* calculations where the MoS_2 gap at hBN-TL decreases by even $-\Delta E_g \sim 500$ meV [43]. On the other hand, MoS_2 gap reduction of $-\Delta E_g \leqslant 50$ meV caused by hBN-SL perfectly agrees with results of above *GW* calculations. It seems that the inclusion of the crystal local field effects in the response of multilayered substrates can significantly modify their polarizability and thereby modify the band gap E_g. Still, the gap reduction of 500 meV caused by an insulating surface is comparable to typical gap reduction caused by metal surfaces [27], which is at least unusual. All spectroscopic measurements (presented in Table II) were performed in ultrahigh vacuum at temperatures; 200 K [2], 77 K [15], 79–299 K [25], 5 K [71], and in Ref. [72] at room temperature.

hBN. The second and third rows in Table III show the $-\Delta E_g$ in hBN caused by adjacent Gr-SL, gr-BL, gr-TL, and gr-∞. The $-\Delta E_g$ in second row is calculated using first approximation, i.e., relative to DFT band gap $E_g = 4.48$ eV, while in third row using second approximation, i.e., relative to G_0W_0 band gap $E_{g(GW)} = 7.3$ eV [73], i.e., $\Delta_g = 2.82$ eV was used. Larger G_0W_0 band gap reduces the hBN polarizability so that the impact of the nearby graphenes is stronger resulting larger $-\Delta E_g$. The fourth row shows the band gap change calculated using supercell G_0W_0 method and AA′ hBN-graphene stacking [73,74], which best matches our model. The $-\Delta E_g$ is calculated relative to G_0W_0 band gaps $E_{g(GW)} = 7.3$ eV

TABLE III. Band gap shifts $-\Delta E_g$ in hBN caused by vicinity of various S-CRYs (listed in first row). (second row) The simulated $-\Delta E_g$ obtained using first approximation [Eq. (76)], i.e., relative to DFT band gap $E_g = 4.48$ eV. (third row) The simulated $-\Delta E_g$ obtained using second approximation [Eq. (77)], i.e., relative to G_0W_0 band gap $E_{g(GW)} = 7.3$ eV [73]. (fourth row) Theoretical $-\Delta E_g$ relative to the G_0W_0 band gaps $E_g = 7.3$ eV [44,73] and $E_g = 7.98$ eV [74]. (fifth row) The experimental $-\Delta E_g$ relative to G_0W_0 band gaps $E_{g(GW)} = 7.3$ eV ($E_{g(GW)} = 7.98$ eV). All band gaps E_g refer to self-standing hBN.

$-\Delta E_g$[meV] in hBN/S-CRY				
S-CRY	Gr-SL	Gr-BL	Gr-TL	Gr-∞
App. 1 Eq. (76)	600	627	627	627
App.2 Eq. (77)	704	747	761	761
Theor.	800 [44] 1075 [73] 800 [74]	930 [74]	980 [74]	
Expt.				500(1180) [75]

[44,73] and $E_{g(GW)} = 7.98$ eV [74], as also pointed out in Table III. It can be noticed that our results slightly underestimate the result of (similar) QEH-$G\Delta W$ method [44], while it significantly underestimates the results of more sophisticated supercell G_0W_0 method [73], that includes a small but perhaps not negligible orbital overlap. Even though the latter method may give a more accurate results, there are still some inconsistencies with the recent STS and optical measurements of hBN at graphite. Namely, by combined STS and optical measurements it was obtained that the band gap in hBN at graphite is $E_{g(EXPT)} = 6.8 \pm 0.2$ eV, and optical gap is ~6.1 eV, providing the exciton binding energy of 0.7 ± 0.2 eV [75]. Similarly, by combined photoluminescence and reflectance spectroscopy measurements it was obtained that the optical gap in hBN on graphite is 6.1 eV [76], which, after adding the 0.7 eV of exciton binding energy, obtained in Ref. [75], provides the band gap of exactly $E_{g(EXPT)} = 6.8$ eV. In both experiments [75,76] measurements were performed in ultrahigh vacuum and in cryogenic conditions ($T \approx 10$ K). According to above-mentioned G_0W_0 band gaps in vacuum, i.e., $E_{g(GW)} = 7.3$ eV and $E_g = 7.98$ eV, the graphite induces the band gap shift between $-\Delta E_g \sim 500$ meV and 1180 meV, respectively, as also shown in fifth row in Table III. Therefore, this obvious inconsistency in theoretical calculations of the band gap in self-standing hBN and the inability to determine it experimentally provides a wide fluctuation of the results for $-\Delta E_g$, but also put our result in the middle of that fluctuation.

We notice that the graphene substrates generally have a very weak impact on the band gap in WS_2 and MoS_2 causing $-\Delta E_g \sim 150$ meV, while the band gap reduction in hBN is $-\Delta E_g \sim 700$ meV. This indicates that TMDs effectively screen the potential produced by the S-CRY and thus protects their electronic states from the influence of the substrate, while this is not the case in hBN.

In order to prove this assumption, below we will compare the spatially dependent induced self-energy of a point charge placed at z_0, which includes the polarizations of both the S-CRY and the 2D-CRY [45]

$$\Delta\Sigma^{S@2D}(z_0) = \frac{1}{2}\int \frac{d\mathbf{Q}}{(2\pi)^2}\Delta W_S(\mathbf{Q}, \omega = 0, z_0, z_0)$$

and which includes only the polarizations of the S-CRY

$$\Delta\Sigma^{S}(z_0) = \frac{1}{2}\int \frac{d\mathbf{Q}}{(2\pi)^2}\Delta V(\mathbf{Q}, \omega = 0)e^{-2|\mathbf{Q}|z_0}. \quad (79)$$

Here $\Delta W_S(z_0, z_0)$ can be obtained by the Fourier transformation of Eq. (73) in z direction, but excluding the crystal local field in x-y plane (i.e., $\mathbf{G}_\parallel = \mathbf{G}'_\parallel = 0$), and $\Delta V(\mathbf{Q}, \omega)$ is given by Eq. (51). Also, one can notice that formula (79) in the perfect screening approximation $\Delta V(\mathbf{Q}, \omega = 0) \approx -v_Q e^{-2|\mathbf{Q}|\Delta}$ (i.e., $D \approx -1$) reduces to image potential $\Delta\Sigma^S(z_0) \approx -1/4(z_0 + \Delta)$. It should be pointed out here that $\Delta\Sigma^{S@2D}$ is not the total but the substrate-induced self-energy, analogous to Eq. (70), i.e., it does not include the direct polarization of 2D-CRY, so that, for example, $\lim_{\Delta\to\infty}\Delta\Sigma^{S@2D}(-L/2 < z_0 < L/2) = 0$. Figure 4 shows the induced self-energies $\Delta\Sigma^S$ (black dashed) and $\Delta\Sigma^{S@2D}$ (blue solid) along [Fig. 4(a)] WS_2-SL and along [Fig. 4(b)] hBN-SL. The cyan dashed line in Fig. 4(a) shows $\Delta\Sigma^{S@2D}$ along MoS_2-SL. The positions of the substrate, which is here Gr-SL, and S, W, Mo, and hBN atomic planes are denoted by vertical dotted lines. It is clearly evident that the presence of WS_2 or MoS_2 significantly reduces the potential produced by Gr-SL, especially inside of 2D-CRYs (between S atoms),

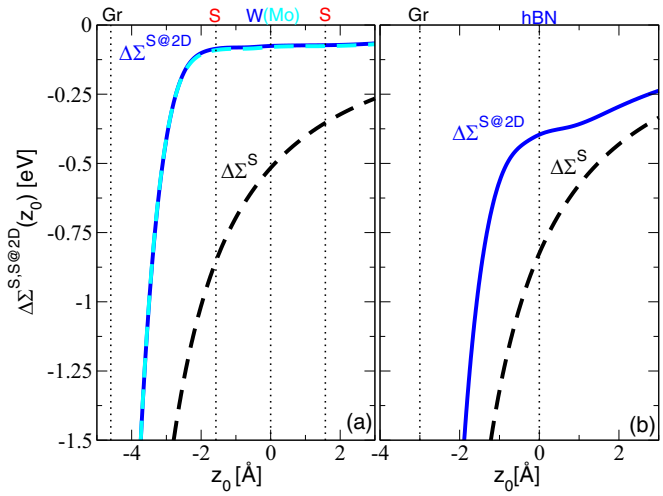

FIG. 4. The substrate-induced self-energies of a point charge $\Delta\Sigma^S$ (black dashed) and $\Delta\Sigma^{S@2D}$ (blue solid) along (a) WS_2-SL and (b) hBN-SL. The cyan dashed line in (a) shows $\Delta\Sigma^{S@2D}$ along MoS_2-SL. The positions of S-CRY, which is here Gr-SL, and S, W, Mo, and hBN atomic planes are denoted by vertical dotted lines. Note that $\Delta\Sigma^S$ does not include, and $\Delta\Sigma^{S@2D}$ includes, the presence of 2D-CRY.

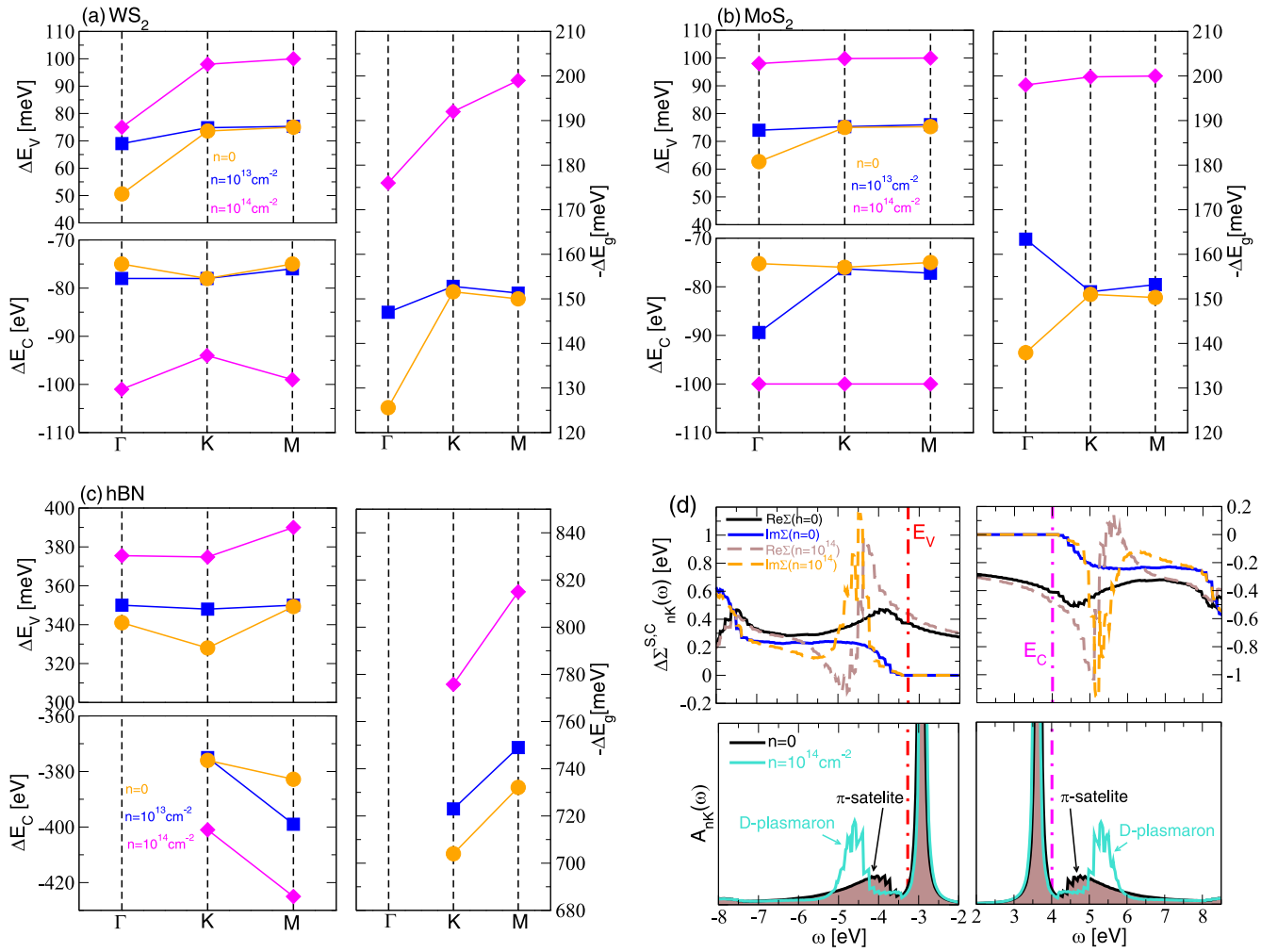

FIG. 5. The valence band shift ΔE_{V}, the conduction band shift ΔE_{C}, and band gap shift $-\Delta E_{\mathrm{g}}$ at Γ, K, and M points of Brillouin zone in (a) WS_2, (b) MoS_2, and (c) hBN caused by nearby doped graphenes. The shifts corresponding to different graphene electron dopings n are denoted by orange dots (●) $n = 0$, blue squares (■) $n = 10^{13}\mathrm{cm}^{-2}$, and magenta diamonds (◆) $n = 10^{14}\mathrm{cm}^{-2}$. (d) The top panels show the induced correlation self-energy $\Delta\Sigma^{\mathrm{C,S}}_{n\mathbf{K}}(\omega)$ in hBN/Gr composite for two graphene dopings $n = 0$ (solid lines) and $n = 10^{14}\mathrm{cm}^{-2}$ (dashed lines) in K point of Brillouin zone. The left and right panels correspond to valence and conduction bands, respectively. The bottom panels in (d) show the spectral functions $A_{n\mathbf{K}}(\omega)$ corresponding to top panels in (d) where the shaded spectra corresponds to pristine ($n = 0$) and unshaded to doped graphene ($n = 10^{14}\mathrm{cm}^{-2}$). The energies of valence and conduction bands, E_V and E_C, at K point, are denoted by dashed-dotted lines.

where, for example, at $z_0 = 0$, $\Delta\Sigma^{\mathrm{S@2D}}/\Delta\Sigma^{\mathrm{S}} \sim 0.15$. It can also be seen that just after entering the TMD, $\Delta\Sigma^{\mathrm{S@2D}}$ saturates at a very small constant value, which means that any orbital extending through the TMD should be well protected from the influence of the substrate screening. This is because TMDs have more pronounced 3D character, in comparison with monoatomic 2D crystals. Namely, the orbital character of the conduction and valence bands is dominated by d orbitals localized on molybdenum or tungsten atoms at $z_0 = 0$. On the other hand if Mo(d) ↔ S(p) electron-hole excitations are more localized in the sulfur layers ($z_0 \approx \pm 1.8$ Å), we can assume that these layers screen and thus protect the inner d orbitals responsible for the semiconductor band gap. The presence of hBN also noticeably reduces the potential $\Delta\Sigma^{\mathrm{S}}$, but that reduction inside of hBN is not as radical as in TMDs, so that at $z_0 = 0$ $\Delta\Sigma^{\mathrm{S@2D}}/\Delta\Sigma^{\mathrm{S}} \sim 0.5$. As already discussed, wide band gap in hBN results its rigid electronic polarization and thus much weaker electronic screening compared to TMDs. For example, static screening in 2D crystals is usually approximated as $W(Q) = v_Q/(1 + \alpha Q)$, where $\alpha = 10$ and 76 in hBN and MoS_2, respectively [30]. This clearly demonstrates strong MoS_2 and weak hBN polarizability. But as already noted, also more pronounced 3D character of TMDs (three atomic layers), results that electrons in TMDs screen the substrate more efficiently than in hBN.

B. Conduction and valence bands shifts $\Delta E_{\mathrm{V,C}}$ along the Brillouin zone

Until now we were looking at the changes of the 2D semiconductor band gap E_g induced by the presence of different substrates. For that we were looking only at the energy shifts of the electron states in the K point of the Brillouin zone. But is this energy shift quantitatively the same along the entire Brillouin zone?

Figures 5(a)–5(c) show the valence band shift ΔE_{V}, the conduction band shift ΔE_{C} and band gap shift $-\Delta E_{\mathrm{g}}$ not only at K but also at Γ and M points of the Brillouin zone in WS_2, MoS_2, and hBN, respectively, caused by nearby doped graphenes. The shifts $\Delta E_{\mathrm{V,C}}$ are defined as difference between the main peaks in electron/hole spectral function (78) and energies $\tilde{E}_{n\mathbf{K}}$ derived in second approximation (77), i.e., using the parameters $\Delta_{\mathrm{g}} = 0.58$, 0.94, and 2.82 eV for WS_2, MoS_2, and hBN, respectively. The shifts corresponding to different graphene electron dopings n are denoted by orange dots (●) $n = 0$, blue squares (■) $n = 10^{13}\mathrm{cm}^{-2}$, and magenta diamonds (◆) $n = 10^{14}\mathrm{cm}^{-2}$. What is common to all systems, but also the expected result, is that the valence band always shifts up $\Delta E_{\mathrm{V}} > 0$, and the conduction band always shifts down $\Delta E_{\mathrm{C}} < 0$, which results the band gap reduction $-\Delta E_{\mathrm{g}} > 0$.

It can be noticed that for fixed doping n the shifts $\Delta E_{\mathrm{V,C}}$ do not change much along the Brillouin zone. However, even though this change is a maximum of ∼20 meV, it can be up to 40% of the total shift (for example ΔE_{V} in Γ and K point for WS_2 and $n = 0$), which makes the rigid shift theory [24] somehow debatable. Mathematically the expression for the self-energy shift $\Delta\Sigma^{\mathrm{C,S}}_{n\mathbf{K}}(\omega)$ (70) (n being here the index of the considered band) has apparently a $\mathbf{K}$ dependence because of the correlation propagator term $\Delta\Gamma^{S}_{\mathbf{GG}'}(\mathbf{Q}, E_{m\mathbf{K}+\mathbf{Q}} - \omega)$, where the $\mathbf{K}$ can not be neglected by redefining $\mathbf{Q}$. Furthermore, Eq. (71) shows how this $\mathbf{K}$ dependence is linked to the variations in $\mathbf{Q}$ in the spectral function $\Delta S^{S}_{\mathbf{GG}'}(\mathbf{Q}, \omega')$ or $\mathrm{Im}W^{S}_{\mathbf{GG}'}(\mathbf{Q}, \omega)$, which can change significantly. In other words, the phase space of real excitations (stored in ΔS), that efficiently contribute to the shifts $\Delta E_{\mathrm{V,C}}$, should change as $\mathbf{K}$ change through the Brillouin zone. However, these energy shifts variations in the WS_2 band structure are very small absolute amounts that are barely within or below the experimental resolution, so that from an experimental point of view the band shifts are rigid. This is especially true for the hBN valence band (visible in ARPES experiments), where the ΔE_{V} change along the zone for only 5% of the total change. Small electronic doping ($n = 10^{13}$ cm^{-2}) causes a negligible raising of the valence band and a negligible lowering of the conduction band. This is expected behavior because already pristine graphene (due to the avalanche of soft interband $\pi \to \pi^*$ transitions) provides strong metallic screening, so that small extra electronic charge does not cause any significant difference. Interestingly, tiny graphene doping still causes 20 meV shifts of valence and/or conduction bands in WS_2 and MoS_2, at the Γ point. Heavy electronic doping ($n = 10^{14}$ cm^{-2}) significantly shifts the valence band up and the conduction band down. For example, in MoS_2 at K point, the valence band raises for additional 25 meV while the conduction band lowers for additional 25 meV resulting in band gap reduction of $-\Delta E_{\mathrm{g}} =$ 200 meV, which is 50 meV larger than in pristine graphene (see also third row and first column in Table II). A similar behavior can be observed for WS_2. However, although these changes (caused by doping) seem large compared to the total nominal change $-\Delta E_{\mathrm{g}}$, compared to the absolute band gap E_{g} they are negligible, i.e., only about 2%. For hBN the similar trend occur; in K point the strong doping rises the valence band for additionally 50 meV and lower the conduction band for additional 25 meV resulting in band gap reduction for additional 75 meV, so that the total band gap shift (induced by doped graphene) is almost $-\Delta E_{\mathrm{g}} = 780$ meV.

As we have already commented, the presence of graphene affects the states in hBN more than the states in TMDs, so below we will consider how graphene affects the spectral properties of valence and conduction electrons in hBN. A similar effect occurs at the M point, and the reduction of the gap increases up to $-\Delta E_{\mathrm{g}} = 820$ meV. The influence on spectral properties of TMD states is very weak, so we do not show it here.

The top panels in Fig. 5(d) show the induced correlation self-energies $\Delta\Sigma^{\mathrm{C,S}}_{n\mathbf{K}}(\omega)$ in hBN/Gr composite for two graphene dopings $n = 0$ (solid lines) and $n = 10^{14}$ cm^{-2} (dashed lines) in K point of Brillouin zone. The left panel corresponds to valence band, and right panel corresponds to conduction band. The bottom panels show the spectral functions corresponding to top panels, where the shaded spectra correspond to pristine ($n = 0$) and unshaded spectra correspond to doped graphene ($n = 10^{14}$ cm^{-2}). The top of the valence band (E_{V}) and the bottom of the conduction band (E_{C}) are denoted by dashed-dotted lines. For pristine graphene, the $\mathrm{Im}\Delta\Sigma^{\mathrm{C,S}}_{n\mathbf{K}}(\omega)$ shows onset, which appears just below the valence band ($\omega \leqslant E_{\mathrm{V}}$) or just above conduction band ($\omega \geqslant E_{\mathrm{C}}$). These onsets are a consequence of the real excitation of the soft $\pi \to \pi^*$ interband electron-hole transitions in graphene. For example, a hole created deeper in the valence band can emit an electron-hole pair in graphene and jump to the upper edge of the valence band. At about 5 eV below E_{V} or above E_{C}, a second onset appears representing the excitation of the graphene π plasmon. For doped graphene $\mathrm{Im}\Delta\Sigma^{\mathrm{C,S}}_{n\mathbf{K}}(\omega)$ shows strong peaks, which appear about 1.0 eV below or above onsets $\omega = E_{\mathrm{V}}$ or $\omega = E_{\mathrm{C}}$, and which are a consequence of the excitation of the Dirac plasmon in graphene. In the quasiparticle spectrum $A_{n\mathbf{K}}$, these structures manifest as satellites, which are labeled as π satellite in the case of pristine graphene and D plasmaron in the case of doped graphene. The position of the satellite can easily be estimated by the following simple approximation. According to Eq. (70), no-recoil approximation $m = n$, plasmon-pole approximation $\Delta S^{\mathrm{S}} \sim \delta(\omega - \omega_Q)$, and if the plasmon has a flat dispersion $\omega_Q = \omega_p$ (e.g., as LO phonon) it is easy to show that the plasmon satellite should appear the most intensively in valence band at $\omega \approx E_{\mathrm{V}} - \omega_p$ and in conduction band at $\omega \approx E_{\mathrm{C}} + \omega_p$. Here the Dirac plasmon has a square-root dispersion $\omega_Q \sim \sqrt{Q}$ and taking into account that its intensity (oscillatory strength) increases with Q, the D-plasmaron intensity should increase much more gradually for $\omega < E_{\mathrm{V}}$ and $\omega > E_{\mathrm{C}}$. Nevertheless, as can be see at bottom panels of Fig. 5(d), the D plasmarons are well separated (about 1.5 eV) from the main peaks.

It should be emphasized here that all these structures are the results of the $G_0\Delta W_{\mathrm{S}}$ theory, however, if one wants to achieve more physical (closer to the experiment) spectral line shapes, it is necessary to carry out a higher-order calculations, e.g., $G_1\Delta W_1^{\mathrm{S}}$, etc. For example, it is expected that the main lines in Fig. 5(d) (bottom panel) will have an asymmetric shape due to the decay into soft intraband ($\pi^* \to \pi^*$) and interband ($\pi \to \pi^*$) transitions in graphene. This does not occur here because (in the lowest $G_0\Delta W_{\mathrm{S}}$ order) the decay into real excitations ($\mathrm{Im}\Delta\Sigma^{\mathrm{C,S}} \neq 0$) starts only for $\omega < E_{\mathrm{V}}$ and

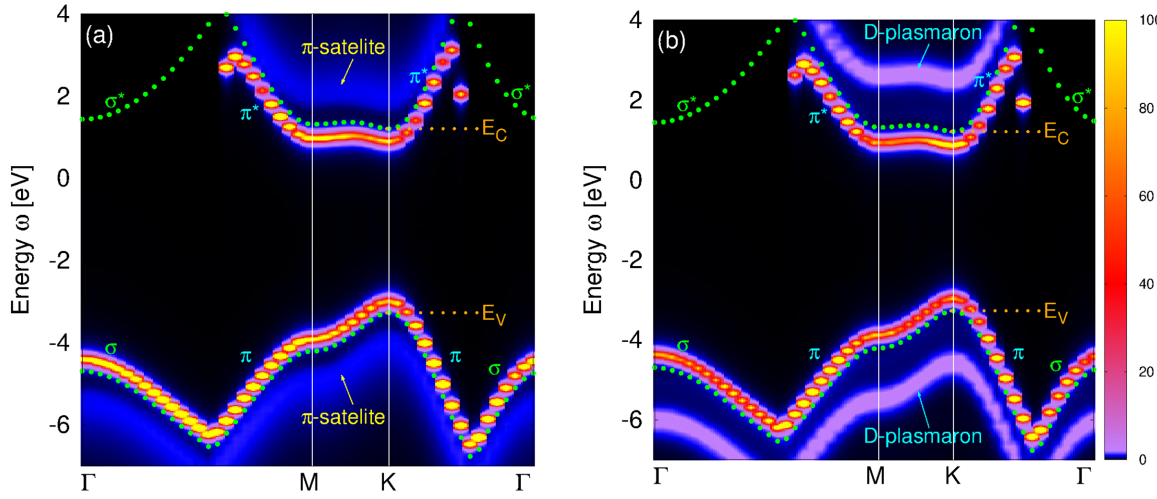

FIG. 6. The spectral intensities $A_{n\mathbf{K}}(\omega)$ of hBN valence and conduction bands along Brillouin zone when hBN is brought into interaction with (a) pristine ($n = 0$) and (b) doped ($n = 1.76 \times 10^{14}\,\mathrm{cm}^{-2}$) graphene. The dotted lines represent the valence and conduction bands in self-standing hBN, i.e., when there is no interaction with graphene.

$\omega > E_C$ [as can be seen in Fig. 5(d), top panels], and the new corrected states are shifted in the gap, above ($\omega > E_V$) and below ($\omega < E_C$), respectively, which means that the new shifted states (because then $\mathrm{Im}\Delta\Sigma^{C,S} = 0$) are infinitely living states (the δ functions rather than asymmetric Lorentzians) [as can be seen in Fig. 5(d), bottom panels]. The more physical result can be achieved in the second iteration, when already corrected Green's function G_1 (in which the corrected energies $E_{V,C} + \Delta E_{V,C}$ are inserted) is used in $\Delta\Sigma_1^{C,S} = iG_1\Delta W_1^S$. Then the new (renormalized) onsets for which $\mathrm{Im}\Delta\Sigma_1^{C,S} \neq 0$ are at $\omega < E_V + \Delta E_V$ and $\omega > E_C + \Delta E_C$, while the new QP energies (because already $G_0\Delta W_S$ provides good shift) are $E_{V,C} + \Delta E_{V,C}^1 \approx E_{V,C} + \Delta E_{V,C}$. Therefore, new corrected V or C state will decay just below or above its energy, respectively, having correct asymmetrical line shape. It should be noted that the above analysis is equally valid if, instead of the initial DFT energies $E_{V,C}$ [approximation (76)], we use already corrected QP energies $\tilde{E}_{V,C}$ [approximation (77)]. It is also possible to carry out more iterations in which the new corrected Green's functions G_2, G_3 are used, although this would probably not significantly correct the result. However, it is a much more complex calculation that goes beyond the scope of this research.

C. Plasmarons in hBN/Gr(n) heterostructures

In this section, we will present the spectral intensities of the valence and conduction bands along the Brillouin zone in the hBN/Gr(n) composite for two marginal graphene dopings $n = 0$ and $n = 1.76 \times 10^{14}\,\mathrm{cm}^{-2}$. We will pay special attention to investigate behavior of satellites, D and π plasmarons, along the Brillouin zone.

Figure 6 shows the spectral intensities (or quasiparticle spectra) of hBN valence and conduction bands when they are brought into interaction with [Fig. 6(a)] pristine and [Fig, 6(b)] doped graphene. Graphene doping is here chosen to be very large, $n = 1.76 \times 10^{14}\,\mathrm{cm}^{-2}$, which usually occur in alkali atoms doped graphene [77]. The dotted lines represent the valence and conduction bands in self-standing hBN, i.e., when the interaction with graphene is switched off. It should be noted that the valence and conduction band change their orbital character, from π (in the region between K and M and beyond) to σ around the Γ point, as also denoted in Fig. 6, thus these segments had to be calculated separately. To limit computational time the σ segment in the conduction band was not calculated.

The spectral intensities in Fig. 6 are calculated using first approximation (76), i.e., relative to DFT band gap $E_g = 4.48\,\mathrm{eV}$. One can notice that when the interaction with graphene is switched on, the main peaks in valence or conduction bands move up or down, respectively. In Fig. 6(a), weakly intense π satellite replicates the entire valence band (very uniformly regardless of its π or σ character), and the same situation occurs in conductive π band. However, it appears that the presence of graphene significantly affects the conducting σ band, or more precisely, it significantly increases the real part of induced self-energy $\mathrm{Re}\Delta\Sigma_{n\mathbf{K}}^{C,S}(\omega)$ resulting a nonphysically large energy shift. This trend can be seen at the discontinuities (where the π and σ bands cross) where the energy shifts are already significantly larger than shifts at M or K points. However, how this effect is still being considered, the spectral line shapes of the conduction σ bands around the Γ point are rather not presented in this paper.

In Fig. 6(b), one can clearly see the D plasmarons, which rigidly (at a distance of about 1.5 eV) follow the valence and conduction bands. It can be noticed that the D plasmaron also reduces the main line spectral weight (between M and K points), relative to the pristine graphene case in Fig. 6(a). So even though very strong graphene doping causes a negligible change of the hBN band gap [e.g., Fig. 5(c) shows that doped graphene reduces the band gap by 75 meV, which is only about 1% of the absolute gap], it causes a noticeable change of the valence and conduction bands spectral line shape so that π satellite turns into D plasmaron, which is also accompanied by the main peak spectral weight reduction. Changes of the spectral line shapes in WS_2 and MoS_2 caused by pristine or doped graphenes are much less pronounced, so there is no need to present these results here.

Finally, it should be noted that in the above spectra only the induced correlation self-energy $\Delta\Sigma^{C,S}_{n\mathbf{K}}$ is included. However, the actual (measurable) line shapes correspond to total correlation self-energy $\Sigma^{C,S}_{n\mathbf{K}} = \Sigma^{C,0}_{n\mathbf{K}} + \Delta\Sigma^{C,S}_{n\mathbf{K}}$, which includes intrinsic decay mechanisms [see Eq. (69)], which can generally overlap with π satelite and D plasmaron and destroy its visibility. Luckily, since in the semiconductors $\mathrm{Im}\Sigma^{C,0}_{n\mathbf{K}} \neq 0$ at $\omega < E_V - E_g$ and $\omega > E_C + E_g$, and since hBN has wide band gap ($E_g > 7$ eV) the overlap between intrinsic satellites and D plasmaron will not occur. This implies that it is very possible that D plasmaron can be measured by ARPES in hBN/Gr composites [36–39], or, e.g., in hBN intercalated by alkali atoms [78].

V. CONCLUSIONS

The proposed $G_0\Delta W_S$ theory is applied to study the valence and conduction bands renormalization in WS_2, MoS_2, and hBN physisorbed at multilayered and doped graphenes. Although our results for band gap shifts $-\Delta E_g$ underestimate other theoretical results, agreement with experimental results is satisfactorily good. It is demonstrated that graphene weakly influences the band gaps in TMDs ($-\Delta E_g \sim 150$ meV), while this change in hBN is more significant ($-\Delta E_g \sim 700$ meV). This effect is proved by performing the calculation of spatially dependent induced self-energy of point charge $\Delta\Sigma^{S@2D}(z_0)$. It is demonstrated that the test charge feels the influence of graphene much less in TMDs than in hBN. Therefore the TMDs provides more efficient electronic screening than hBN resulting very weak renormalization (or protection) of the conduction and valence bands in TMDs and finally very small $-\Delta E_g \leqslant 150$ meV. We also point out that semiconducting substrates such as SiO_2 or hBN have a negligible effect on the TMD band structure ($-\Delta E_g \leqslant 50$ meV), of course only in case of vdW binding between TMD and substrate. Multiplication of graphene layers in S-CRY or graphene doping insignificantly affect the energy shift of valence and conduction bands. Also, it is shown that the valence and conduction bands shifts through Brillouin zone are nonrigid but small.

The spectral lines shapes of valence and conduction bands in the hBN interacting with pristine and doped graphenes are calculated. It is shown that the presence of graphene introduces satellites, which replicate the valence and conduction bands. Pristine graphene introduces weak π satellites (result of the excitation of soft interband $\pi \to \pi^*$ transitions) while doped graphene introduces more intensive D plasmaron (result of the excitation of Dirac plasmon), which could potentially be seen in ARPES measurements.

ACKNOWLEDGMENTS

The authors acknowledge financial support from Croatian Science Foundation (Grant No. IP-2020-02-5556) as well as support from European Regional Development Fund for the "QuantiXLie Centre of Excellence" (Grant No. KK.01.1.1.01.0004). The authors are grateful to Dino Novko for useful discussions.

[1] B. Radisavljevic, A. Radenovic, J. Brivio, V. Giacometti, and A. Kis, Nature Nanotechnol. **6**, 147 (2011).
[2] M. I. B. Utama, H. Kleemann, W. Zhao, C. S. Ong, F. H. da Jornada, D. Y. Qiu, H. Cai, H. Li, R. Kou, S. Zhao *et al.*, Nature Electron. **2**, 60 (2019).
[3] G. Fiori, F. Bonaccorso, G. Iannaccone, T. Palacios, D. Neumaier, A. Seabaugh, S. K. Banerjee, and L. Colombo, Nature Nanotechnol. **9**, 768 (2014).
[4] F. Wu, H. Tian, Y. Shen, Z. Hou, J. Ren, G. Gou, Y. Sun, Y. Yang, and T.-L. Ren, Nature (London) **603**, 259 (2022).
[5] F. Bonaccorso, Z. Sun, T. Hasan, and A. Ferrari, Nature Photon. **4**, 611 (2010).
[6] J. Wang, X. Mu, M. Sun, and T. Mu, Appl. Mater. Tod. **16**, 1 (2019).
[7] J. Wang, Z. Xing, X. Chen, Z. Cheng, X. Li, and T. Liu, Front. Phys. **8**, 37 (2020).
[8] F. Koppens, T. Mueller, P. Avouris, A. Ferrari, M. Vitiello, and M. Polini, Nature Nanotechnol. **9**, 780 (2014).
[9] H. Hu, X. Yang, X. Guo, K. Khaliji, S. R. Biswas, F. J. García de Abajo, T. Low, Z. Sun, and Q. Dai, Nature Commun. **10**, 1131 (2019).
[10] T. Mueller and E. Malic, npj 2D Mater. Applic. **2**, 29 (2018).
[11] T. Low, A. Chaves, J. D. Caldwell, A. Kumar, N. X. Fang, P. Avouris, T. F. Heinz, F. Guinea, L. Martin-Moreno, and F. Koppens, Nature Mater. **16**, 182 (2017).
[12] G. Zhang, S. Huang, A. Chaves, C. Song, V. O. Özçelik, T. Low, and H. Yan, Nature Commun. **8**, 14071 (2017).
[13] S. Tongay, H. Sahin, C. Ko, A. Luce, W. Fan, K. Liu, J. Zhou, Y.-S. Huang, C.-H. Ho, J. Yan *et al.*, Nature Commun. **5**, 3252 (2014).
[14] M. R. Molas, K. Nogajewski, A. O. Slobodeniuk, J. Binder, M. Bartos, and M. Potemski, Nanoscale **9**, 13128 (2017).
[15] Y. L. Huang, Y. Chen, W. Zhang, S. Y. Quek, C.-H. Chen, L.-J. Li, W.-T. Hsu, W.-H. Chang, Y. J. Zheng, W. Chen *et al.*, Nature Commun. **6**, 6298 (2015).
[16] H. J. Conley, B. Wang, J. I. Ziegler, R. F. Haglund Jr, S. T. Pantelides, and K. I. Bolotin, Nano Lett. **13**, 3626 (2013).
[17] C. Wang, Q. He, U. Halim, Y. Liu, E. Zhu, Z. Lin, H. Xiao, X. Duan, Z. Feng, R. Cheng *et al.*, Nature (London) **555**, 231 (2018).
[18] A. Raja, A. Chaves, J. Yu, G. Arefe, H. M. Hill, A. F. Rigosi, T. C. Berkelbach, P. Nagler, C. Schüller, T. Korn *et al.*, Nature Commun. **8**, 15251 (2017).
[19] A. Chaves, J. G. Azadani, H. Alsalman, D. Da Costa, R. Frisenda, A. Chaves, S. H. Song, Y. D. Kim, D. He, J. Zhou *et al.*, npj 2D Mater. Applic. **4**, 29 (2020).
[20] D. Y. Qiu, F. H. da Jornada, and S. G. Louie, Nano Lett. **17**, 4706 (2017).
[21] S. Park, N. Mutz, T. Schultz, S. Blumstengel, A. Han, A. Aljarb, L.-J. Li, E. J. List-Kratochvil, P. Amsalem, and N. Koch, 2D Mater. **5**, 025003 (2018).
[22] J. Ryou, Y.-S. Kim, S. Kc, and K. Cho, Sci. Rep. **6**, 29184 (2016).

[23] D. Tebbe, M. Schütte, K. Watanabe, T. Taniguchi, C. Stampfer, B. Beschoten, and L. Waldecker, npj 2D Mater. Applic. **7**, 29 (2023).

[24] L. Waldecker, A. Raja, M. Rösner, C. Steinke, A. Bostwick, R. J. Koch, C. Jozwiak, T. Taniguchi, K. Watanabe, E. Rotenberg *et al.*, Phys. Rev. Lett. **123**, 206403 (2019).

[25] C. Zhang, A. Johnson, C.-L. Hsu, L.-J. Li, and C.-K. Shih, Nano Lett. **14**, 2443 (2014).

[26] M. M. Ugeda, A. J. Bradley, S.-F. Shi, F. H. Da Jornada, Y. Zhang, D. Y. Qiu, W. Ruan, S.-K. Mo, Z. Hussain, Z.-X. Shen *et al.*, Nature Mater. **13**, 1091 (2014).

[27] N. Zibouche, M. Schlipf, and F. Giustino, Phys. Rev. B **103**, 125401 (2021).

[28] M. H. Naik and M. Jain, Phys. Rev. Mater. **2**, 084002 (2018).

[29] M. Drüppel, T. Deilmann, P. Krüger, and M. Rohlfing, Nature Commun. **8**, 2117 (2017).

[30] Z. Rukelj and V. Despoja, New J. Phys. **22**, 063052 (2020).

[31] A. Guandalini, P. D'Amico, A. Ferretti, and D. Varsano, npj Comput. Mater. **9**, 44 (2023).

[32] D. Y. Qiu, F. H. da Jornada, and S. G. Louie, Phys. Rev. Lett. **111**, 216805 (2013).

[33] R. R. Pela, C. Vona, S. Lubeck, B. Alex, I. G. Oliva, and C. Draxl, arXiv:2310.04198.

[34] F. A. Rasmussen and K. S. Thygesen, J. Phys. Chem. C **119**, 13169 (2015).

[35] B. Zhu, X. Chen, and X. Cui, Sci. Rep. **5**, 9218 (2015).

[36] C. Chen, J. Avila, S. Wang, Y. Wang, M. Mucha-Kruczyński, C. Shen, R. Yang, B. Nosarzewski, T. P. Devereaux, G. Zhang *et al.*, Nano Lett. **18**, 1082 (2018).

[37] E. Wang, X. Lu, S. Ding, W. Yao, M. Yan, G. Wan, K. Deng, S. Wang, G. Chen, L. Ma *et al.*, Nature Phys. **12**, 1111 (2016).

[38] E. Wang, G. Chen, G. Wan, X. Lu, C. Chen, J. Avila, A. V. Fedorov, G. Zhang, M. C. Asensio, Y. Zhang *et al.*, J. Phys.: Condens. Matter **28**, 444002 (2016).

[39] J. Jobst, A. J. Van der Torren, E. E. Krasovskii, J. Balgley, C. R. Dean, R. M. Tromp, and S. J. Van der Molen, Nature Commun. **7**, 13621 (2016).

[40] K. Andersen, S. Latini, and K. S. Thygesen, Nano Lett. **15**, 4616 (2015).

[41] Y. Cho and T. C. Berkelbach, Phys. Rev. B **97**, 041409(R) (2018).

[42] M. Rohlfing, Phys. Rev. B **82**, 205127 (2010).

[43] O. Adeniran and Z.-F. Liu, Phys. Rev. Mater. **7**, 054001 (2023).

[44] K. T. Winther and K. S. Thygesen, 2D Mater. **4**, 025059 (2017).

[45] V. Despoja, D. J. Mowbray, D. Vlahović, and L. Marušić, Phys. Rev. B **86**, 195429 (2012).

[46] L. Hedin, Phys. Rev. **139**, A796 (1965).

[47] G. Strinati, Phys. Rev. B **29**, 5718 (1984).

[48] M. S. Hybertsen and S. G. Louie, Phys. Rev. B **34**, 5390 (1986).

[49] M. Rohlfing and S. G. Louie, Phys. Rev. Lett. **81**, 2312 (1998).

[50] M. Rohlfing and S. G. Louie, Phys. Rev. B **62**, 4927 (2000).

[51] G. Onida, L. Reining, and A. Rubio, Rev. Mod. Phys. **74**, 601 (2002).

[52] J. B. Neaton, M. S. Hybertsen, and S. G. Louie, Phys. Rev. Lett. **97**, 216405 (2006).

[53] S. Ismail-Beigi, Phys. Rev. B **73**, 233103 (2006).

[54] C. A. Rozzi, D. Varsano, A. Marini, E. K. U. Gross, and A. Rubio, Phys. Rev. B **73**, 205119 (2006).

[55] V. Despoja, T. Djordjević, L. Karbunar, I. Radović, and Z. L. Mišković, Phys. Rev. B **96**, 075433 (2017).

[56] V. Despoja, Z. Rukelj, and L. Marušić, Phys. Rev. B **94**, 165446 (2016).

[57] J. Li, G. D'Avino, I. Duchemin, D. Beljonne, and X. Blase, Phys. Rev. B **97**, 035108 (2018).

[58] I. Duchemin, D. Jacquemin, and X. Blase, J. Chem. Phys. **144**, 164106 (2016).

[59] I. Duchemin, C. A. Guido, D. Jacquemin, and X. Blase, Chem. Sci. **9**, 4430 (2018).

[60] D. Amblard, G. D'Avino, I. Duchemin, and X. Blase, Phys. Rev. Mater. **6**, 064008 (2022).

[61] M. Winter, M. H. E. Bousquet, D. Jacquemin, I. Duchemin, and X. Blase, Phys. Rev. Mater. **5**, 095201 (2021).

[62] Z.-F. Liu, F. H. da Jornada, S. G. Louie, and J. B. Neaton, J. Chem. Theory Comput. **15**, 4218 (2019).

[63] D. Y. Qiu, F. H. da Jornada, and S. G. Louie, Phys. Rev. B **103**, 045117 (2021).

[64] P. Giannozzi, S. Baroni, N. Bonini, M. Calandra, R. Car, C. Cavazzoni, D. Ceresoli, G. L. Chiarotti, M. Cococcioni, I. Dabo *et al.*, J. Phys.: Condens. Matter **21**, 395502 (2009).

[65] N. Troullier and J. L. Martins, Phys. Rev. B **43**, 1993 (1991).

[66] D. R. Hamann, Phys. Rev. B **88**, 085117 (2013).

[67] J. P. Perdew, K. Burke, and M. Ernzerhof, Phys. Rev. Lett. **77**, 3865 (1996).

[68] H. J. Monkhorst and J. D. Pack, Phys. Rev. B **13**, 5188 (1976).

[69] Y. Baskin and L. Meyer, Phys. Rev. **100**, 544 (1955).

[70] V. L. Solozhenko, G. Will, and F. Elf, Solid State Commun. **96**, 1 (1995).

[71] C. Murray, W. Jolie, J. A. Fischer, J. Hall, C. van Efferen, N. Ehlen, A. Grüneis, C. Busse, and T. Michely, Phys. Rev. B **99**, 115434 (2019).

[72] X. Liu, I. Balla, H. Bergeron, G. P. Campbell, M. J. Bedzyk, and M. C. Hersam, ACS Nano **10**, 1067 (2016).

[73] K. S. Thygesen, 2D Mater. **4**, 022004 (2017).

[74] P. Wang, W. Lee, J. P. Corbett, W. H. Koll, N. M. Vu, D. A. Laleyan, Q. Wen, Y. Wu, A. Pandey, J. Gim *et al.*, Adv. Mater. **34**, 2201387 (2022).

[75] R. J. P. Román, F. J. C. Costa, A. Zobelli, C. Elias, P. Valvin, G. Cassabois, B. Gil, A. Summerfield, T. S. Cheng, C. J. Mellor *et al.*, 2D Mater. **8**, 044001 (2021).

[76] C. Elias, P. Valvin, T. Pelini, A. Summerfield, C. Mellor, T. Cheng, L. Eaves, C. Foxon, P. Beton, S. Novikov *et al.*, Nature Commun. **10**, 2639 (2019).

[77] L. Marušić and V. Despoja, Phys. Rev. B **95**, 201408(R) (2017).

[78] I. Lončarić, Z. Rukelj, V. M. Silkin, and V. Despoja, npj 2D Materials and Applications **2**, 33 (2018).